Designing Robust Liquid and Solid Repellent Surfaces

by

Mathew Boban

A dissertation submitted in partial fulfillment
of the requirements for the degree of
Doctor of Philosophy
(Macromolecular Science and Engineering)
in the University of Michigan
2018

Doctoral Committee:

Associate Professor Anish Tuteja, Chair
Assistant Professor Neil P. Dasgupta
Professor Jinsang Kim
Assistant Professor Geeta Mehta

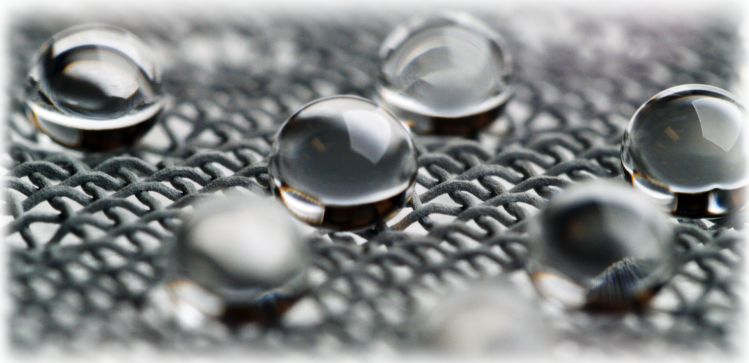

Mathew Boban

mboban@umich.edu

ORCiD: 0000-0001-5851-9225

DEDICATION

To My Parents

ACKNOWLEDGMENTS

Firstly, I thank my research advisor, Prof. Anish Tuteja, who has driven me to explore the limits of what is possible. He has enabled me to work on fascinating scientific and engineering challenges that are focused on societal benefit. Thanks also to my committee members, Prof. Jinsang Kim, Prof. Geeta Mehta, Prof. Neil Dasgupta, and former member Prof. Peter Green for supporting my development as a student and researcher, for sharing materials and equipment, and for valuable input on my dissertation. Significant portions of this work resulted from collaborations with Prof. Mehta (and her lab members, Shreya and Pooja), Prof. Dasgupta (and his students, Ashley and Eric), as well as Prof. Steve Ceccio, Prof. Marc Perlin, and James Gose.

I owe a great deal to members of the Polymers, Surfaces, and Interfaces research group. Spending time with you all, while working hard or hardly working, has been the happiest part of the last few years. Much of this work was undertaken jointly with Kevin and Chao. Sarah and Catherine, your support helped me bear the toughest times and I owe you more than I could repay. Ethan, I'll miss all the time we spent commiserating or sharing anecdotes. To those following me – Dhyani, Brian, Alex, and Brian – I know any work I leave unfinished will be in good hands. I also thank other members of the groups that worked diligently with me or taught me valuable skills, including: Duck Hyun, Raghu, Sai, Gibum, An, Inseong, Omkar, Charlotte, and Daniel. I also thank all my other friends, including Ahmet, Amey, Harry, Ryan, Brad, Max, Ayse, and Caymen, to name but a few. We've eaten, drank, and been merry together, and I'll miss you all.

It's been a pleasure to belong to the Macro program. The administrators, Adam and Nonna, have been unceasingly supportive. The faculty and students are always generous with their time and expertise. This work was supported by several institutions, including the Air Force Research Laboratory, the Office of Naval Research, and the National Science Foundation. Specific notes are included in individual chapters. I also thank PPG Industries for a fellowship. I'd also like to thank all the staff at the Biointerfaces Institute, the Michigan Materials and Characterization Lab, the Lurie Nanofabrication Laboratory, and the Van Vlack Laboratory for their diligent efforts to maintain our excellent facilities.

Lastly, and most importantly, I thank all of my family for their unwavering love and support. This work would not exist without their faith.

TABLE OF CONTENTS

LIST OF FIGURES

LIST OF TABLES

ABSTRACT

Surfaces that remain uncontaminated by liquids and solids have been investigated over the last two decades to address numerous disparate engineering challenges. The applications for such materials include: self-cleaning surfaces, drag-reducing coatings for ships, fog-resistant windows, efficient heat exchangers, ice-shedding wind turbines and powerlines, membranes that allow for facile clean-up of oil spills, and inexpensive microfluidic diagnostic devices. Researchers have employed a multitude of approaches, such as textured porous solids that entrap air, lubricant-infused surfaces, covalently attached monolayers, or compliant elastomers, to effectively repel high- and low-surface tension liquids including water, oils, and solvents, as well as undesired solid materials including ice, dirt, and minerals. However, the limited longevity of these surfaces has impeded their widespread usage. Damaging environmental conditions, such as mechanical abrasion, elevated temperature, ultraviolet light, harsh solvents, extended immersion under elevated liquid pressure, and micro-organisms, can all rapidly degrade the functionality of these materials in the real world.

This dissertation presents the systematic design of liquid- and solid-repellent surfaces with improved resistance to these damaging conditions, and explores some of their applications. The first research chapter outlines a novel fabrication methodology for hyperbranched, hierarchical nanowire structures with independently controllable geometry at each length scale. This novel process was utilized for the fabrication of superomniphobic surfaces with low adhesion to very low-surface-tension liquids, such as heptane. These surfaces also demonstrated high resistance to wetting under pressure. The next three chapters discuss the systematic design of repellent surfaces which are more scalable, and resist a broader range of damaging conditions. The first demonstrates the methodical identification of spray-coating formulations that produce mechanically robust and thermally healable superhydrophobic surfaces, based on the optimization of partial miscibility between hydrophobic small molecules and polymer matrices. These coatings far exceeded the durability of commercial superhydrophobic coatings, and are being adapted for marine drag reduction applications.

Though exceptionally durable, the superhydrophobic coatings were not capable of repelling low-surface-tension liquids (*i.e.*, not "superomniphobic") and were not transparent. To address these limitations and improve on the limited lifetime of existing superomniphobic or omniphobic surfaces, a smooth, transparent, substrate-independent "omniphobic" coating was also developed. Optimization of phase-separation was used again to maximize the repellency and abrasion resistance of the coatings. Lastly, covalently-attached polydimethylsiloxane thin films, deposited using a fast and facile vapor-phase methodology, were shown to repel even ultra-low-surface-tension fluorinated liquids, as well as a variety of solids, such as marine algae. These films exhibited high liquid mobility and low solid adhesion forces due to their liquid-like nature. Due to their thermal stability and conductivity, these films are promising for heat-transfer applications, particularly for facilitating efficient drop-wise condensation of low-surface-tension solvents, which has not been extensively studied.

The following three chapters discuss inexpensive open-channel microfluidic devices fabricated from pressure-resistant superomniphobic fluorinated paper or superhydrophobic/oleophobic textured silicon. These devices could even confine fast-flowing low-surface-tension liquids, such as hexane. This enabled the first demonstration, in open-channel devices, of the chemical lysis and detection of *E. coli* bacteria and the fabrication of hydrophilic or hydrophobic polymer microparticles via flow-focusing emulsification. The final chapter reports novel superhydrophobic cell-culture vessels that readily generated spheroidal cancer cell colonies for *in vitro* biological studies and therapeutic assays. This methodology improved replication of physiological conditions compared to conventional two-dimensional culture techniques, while providing greater stability than state-of-the-art hanging drop plates.

CHAPTER 1

Introduction

1.1 Introductory Remarks

Liquid-repellent surfaces have recently garnered much attention for their applications in self-cleaning paints,[1] marine drag reduction,[2] stain resistant clothing,[3] and oil-water separation.[4] There are numerous methods to reduce a surface's interactions with a wide range of liquids, to the point that droplets readily roll or slide from it when it is inclined.

Superhydrophobic surfaces (SHSs), which imitate the leaves of the lotus plant (*Nelumbo nucifera*), combine rough surface texture with non-wetting surface chemistry to cause the entrapment of micro-pockets of air beneath contacting water. The water beads up into nearly-spherical droplets which can readily bounce off the surface.[1] The addition of re-entrant microscale geometry can also enable the repulsion of a broad range of lower-surface-tension liquids, such as oils or organic solvents, yielding "superomniphobic" surfaces (SOSs).[5,6] To improve the pressure resistance, one may replace the air in rough textured surfaces with a preferentially wetting non-volatile lubricant, causing most immiscible contacting liquids to slide readily from the surface.[7,8] Finally, liquid-repellent smooth surfaces may be produced by chemical modification with densely packed monolayers of low surface energy molecules, spin coating, or polymer grafting.[9–13] Over the last several decades, numerous examples of surfaces with high liquid repellency have been demonstrated using one of these general strategies.

However, each of these approaches has distinct drawbacks hindering its widespread adoption and/or liquid repellency. This thesis primarily focuses on addressing these drawbacks with these approaches that limit their ability to produce robust surfaces. These surfaces fabricated in this work successfully withstood a broad variety of harsh environmental conditions, and show promise in applications such as marine drag reduction and condensation heat transfer. Some of the resulting surfaces are also capable of resisting the adhesion of various solid contaminants, greatly increasing their versatility.

1.2 Wettability on Smooth and Textured Surfaces

The wettability of a liquid on a surface is easily quantified by observing the contact angle θ, at the base of the droplet (Figure 1.1). Liquids of varying surface tension and polarity exhibit a broad range of interactions with surfaces depending on their roughness, surface energy, and chemical homogeneity, from completely spreading into a thin film ($\theta \approx 0°$) to completely beading up into a perfectly spherical, mobile droplet ($\theta \approx 180°$) (Figure 1.2).

By utilizing carefully engineered micro- /nano-texture and surface chemistry, one can selectively induce these wettabilities with liquids with varying surface tensions and polarities. One may also geometrically pattern these surface properties to independently spatially confine different liquids at various length scales.

1.2.1 Equilibrium Contact Angle and Surface Tension

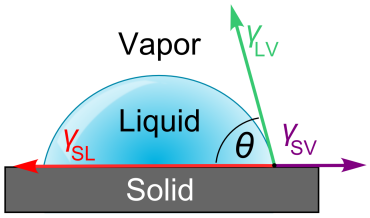

Figure 1.1: A liquid droplet sitting on a smooth, chemically homogeneous surface theoretically exhibits an equilibrium intrinsic contact angle, θ_E, which is determined by the balance of the surface tension forces acting on the three-phase contact line at the base of the droplet.

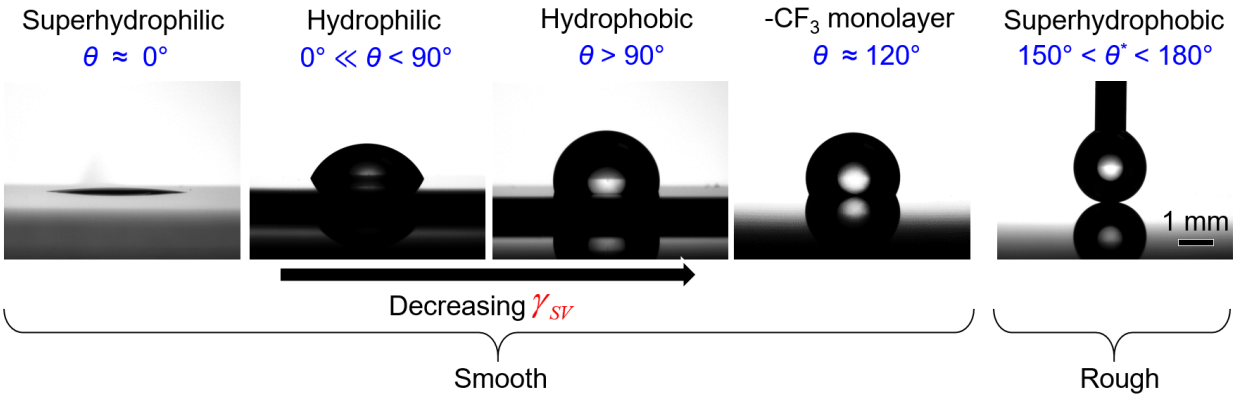

Figure 1.2: The conventional contact angle ranges for describing wetting behavior. These are representative images taken from a contact angle goniometer of water droplets on a broad range of surfaces. The four on the left are smooth surfaces with decreasing surface energy: plasma-cleaned glass, polycaprolactone, polydimethylsiloxane, and spin-coated fluorodecyl POSS (see Chapter 4). The surface on the far right is a near-perfect superhydrophobic surface, silicon nanograss treated with perfluorodecyltrichlorosilane, with $\theta >$ 170° and $\Delta\theta \approx 0°$ (see Chapter 8). Equivalent terms exist for describing behavior with oils ("oleo-") and other low γ_{LV} liquids ("omni-").

Table 1.1: The surface tension of the various liquids used throughout this work. Values are taken from [8, 15–17]

Liquid	γ_{LV} (mN/m)
Water	72.1
Diidomethane	67.0
Formamide	57.0
Propylene glycol	45.6
Chloroform	26.7
n-Hexadecane	27.5
n-Decane	23.4
n-Octane	21.1
n-Hexane	17.9
Toluene	27.9
Ethanol	22.1
1-Propanol	20.9
2-Propanol	23.3
Methanol	22.1
Acetone	23.5
Polydimethyl siloxane	19.9
Krytox 100	16.0
Methoxyperfluorobutane	13.0

This equilibrium contact angle is related to the surface energy balance between the solid-vapor, liquid-vapor, and solid-liquid interfaces, as described by Young's equation[14]

$$\cos\theta_E = \frac{\gamma_{SV} - \gamma_{SL}}{\gamma_{LV}} \tag{1.1}$$

where θ_E is the equilibrium intrinsic contact angle that a liquid with surface tension γ_{LV} exhibits on a solid with surface energy γ_{SV} and a solid-liquid interfacial tension γ_{SL}. Table 1.1 lists surface tension values for various liquids, including those used in this work. Table 1.2 lists surface energy values for selected solids.

The γ_{LV} is generally simple to measure via a variety of methods, including the pendant drop method, in which a liquid with known density is suspended from a needle such that its shape is controlled by the opposing forces of gravity and surface tension. A numerical fit to its profile is then used to calculate its surface tension using the Young-Laplace equation.[19] This may also be extended to interfacial tension between two liquids, if the pendant drop is immersed in another liquid, which is useful for studies of emulsions, for example.[20]

The γ_{SV} may be characterized by measuring the contact angles of one or more liquids of known surface tension. A relatively crude, but very simple, technique is the Zisman method. The contact angles of series of chemically similar liquids with varying surface tension (for example, linear alkanes of varying length) are measured, and the intercept of the linear fit yields the highest γ_{LV}

Table 1.2: The approximate surface energies of various solids. Values are taken from [17, 18]

Solid	γ_{SV} (mJ/m^2)
CF_3 monolayer	9
CH_3 monolayer	23
Polytetrafluoroethylene	19
Polypropylene	31
Polystyrene	34
Poly(methyl methacrylate)	41
Cellulose	89
Glass	~310
Titanium dioxide	~530
Silicon oxide	~1240

liquid that would yield θ=0°, or an approximation of the solid surface energy. This estimate of γ_{SV} is referred to as the critical surface tension (γ_c).[21] Over the last few decades, numerous refinements have been made to account for the specific interactions between solids and liquids, including polar and dispersion bonding. The simplest of these is the Fowke's method, which uses the contact angles determined with one polar liquid (typically water) and one non-polar liquid (typically diiodomethane or hexadecane), with known dispersive and polar surface tension components, to infer γ_{SV}. This method is reasonably accurate for relatively low-surface energy materials, such as hydrophobic polymers, as long as they do not wet with the non-polar probe liquid. High surface energy materials such as clean ceramics and metals are far more difficult to accurately measure and reported values in the literature vary widely. Very high surface energy solid materials are extremely prone to accumulating a molecular layer of lower surface energy contaminants if not stored in an ultra-high vacuum environment.[22] This makes it nearly impossible to measure them in their native state, and experimentally determined values may diverge widely from theoretical values.[17] Finally, from measured γ_{LV} and γ_{SV} values for a solid-liquid pair, one may infer the γ_{SL} depending on the contact angles.

From equation 1.1, one may conclude that liquids exhibiting low surface tension (γ_{LV}) such as ethanol (γ_{LV} = 22 mN/m versus 72 mN/m for water) are generally more prone to spreading into a thin film on a given solid material, as this is energetically favorable. Similarly, a liquid with a given γ_{LV} exhibits higher contact angles on a surface with lower γ_{SV}. In the case of water, surfaces are termed hydrophilic when $\theta_E < 90$ °, and hydrophobic when $\theta_E > 90$°. For a smooth surface, the maximum intrinsic contact angle with water is $\theta_E \approx 120$°, which occurs on a perfluorinated monolayer with $\gamma_{SV} \approx 9$ J/m^2, somewhat higher than the often cited critical surface tension determined by Zisman ($\gamma_c \approx 6$ J/m^2).[21,23] Fluorinated monolayers are the most liquid repellent, as fluorine is the most electronegative element and has limited polarizability. This minimizes intermolecular forces between a dense trifluoromethylated surface and any contacting liquid.[24] There are no known materials that

exhibit $\theta_E > 90°$ with liquids with $\gamma_{LV} \lesssim 40$ mN/m.[5]

1.2.2 Contact Angle Hysteresis and Sliding Angle

In practice, a single equilibrium contact angle is very rarely observed. Virtually all surfaces exhibit some chemical heterogeneity or physical roughness, which causes local variations in the liquid-solid adhesion and therefore variation in the contact angle.[25–28] Reproducibly measuring static contact angles is also highly challenging. Typically, the drop will adopt just one of many metastable states close to the equilibrium contact angle, biased by exactly how the drop is deposited on the surface – for example, whether or not the drop is pushed into or pulled away from the surface.[29]

For the purpose of comparing surfaces, it is preferable to measure and report the complete range of metastable contact angles possible on the surface. That is, the dynamic contact angles as measured by the sessile drop technique (Figure 1.3).[30] A droplet is held simultaneously in contact with a microsyringe and the surface. Liquid is gradually added to the droplet until the contact line begins to move outward at a constant contact angle – this is the advancing contact angle, θ_a. Then liquid is slowly withdrawn from the droplet until the contact line moves inward at a constant receding contact angle, θ_r. The difference between the two is referred to as the contact angle hysteresis ($\Delta\theta = \theta_a - \theta_r$). The exact relationship between θ_a, θ_r, and θ_E is complex and dependent on the specific properties of the surface.[26]

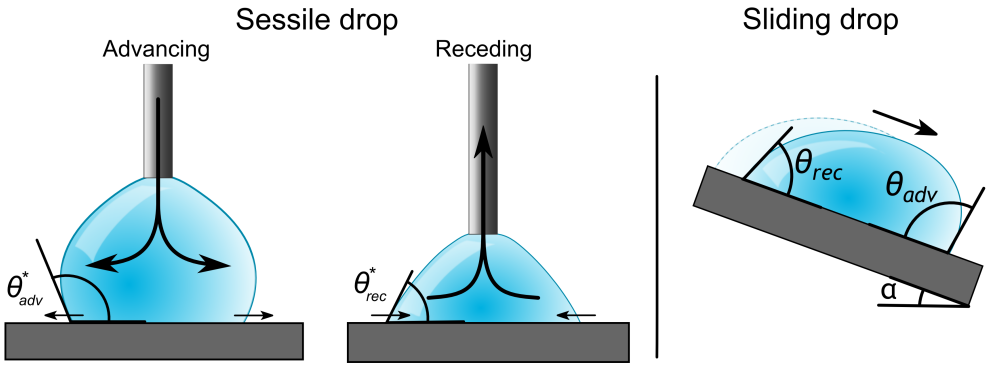

Figure 1.3: A range of contact angles may be measured on most substrates, from the receding angle to the advancing angle, observed on a sessile drop which is expanded/contracted or on a drop which is sliding on an inclined surface.

Generally, smooth uniform surfaces with repellent chemistry (composed of alkyl, fluoroalkyl, or methylsiloxane functional groups) or textured surfaces with robust composite interfaces (see Section 1.2.3.2 below) will exhibit the lowest $\Delta\theta$. Minimal $\Delta\theta$ maximizes the droplet mobility – a $\Delta\theta \approx 0°$ indicates that the surface has very few energetic barriers to droplet motion.[31] This relationship between the hysteresis and the angle a substrate must be tilted to allow a droplet to slide is reasonably well captured by the simple Furmidge relation for smooth surfaces.[25,32]

$$\sin\alpha = \frac{\gamma_{LV} w}{mg}(\cos\theta_r - \cos\theta_a) \tag{1.2}$$

where w is the width of the droplet, γ_{LV} is the surface tension of the liquid, m is the mass of the droplet, g is the acceleration due to gravity, and α is the sliding angle (Figure 1.3).

1.2.3 Wetting on Textured Surfaces

1.2.3.1 Wenzel

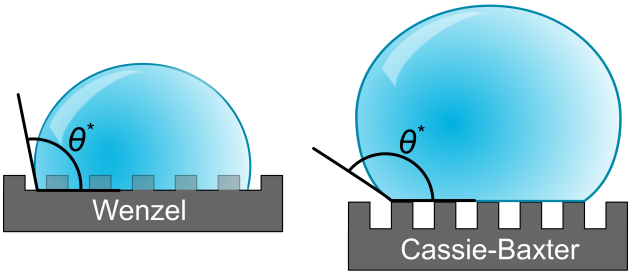

Figure 1.4: The possible wetting states on rough surfaces with features smaller than the capillary length of the liquid are: the fully wetted Wenzel state, in which the liquid fully penetrates into the surface texture, or the composite Cassie-Baxter state, in which air pockets are entrapped beneath the liquid. Typically the apparent contact angle θ^* is greater on the latter, and the droplets are more mobile.

The effect of roughness on wettability was shown in the early 20$^{\text{th}}$ century to follow what is now referred to as the Wenzel equation[33]

$$\cos\theta^* = r\cos\theta_E, \tag{1.3}$$

Following this relation, the macroscopic apparent contact angle θ^* is the intrinsic contact angle of the surface material enhanced by the surface roughness. That is to say, a roughened "philic" material ($\theta_E < 90°$) exhibits a decreased contact angle, which may even approach 0°. A roughened "phobic" material ($\theta_E > 90°$) exhibits an increase in contact angle. However, in either case, an increase in r inevitably increases the solid-liquid contact area, and also increases the length and tortuosity of the contact line. This inevitably increases the $\Delta\theta$, and droplets in the Wenzel state on rough surfaces are generally completely immobile, with θ_r approaching 0°. One notable exception is when the surface texture is conformally coated with a liquid lubricant.[34]

1.2.3.2 Cassie-Baxter

Certain surfaces may be sufficiently rough and be composed of materials with sufficiently low surface energy to enable microscale air pockets to be entrapped beneath the liquid (Figure 1.4). This is known as a composite wetting state, or the Cassie-Baxter state.[35] The apparent macroscopic contact angle is then effectively a weighted average of the contact angles of the liquid on the wetted solid and the air pockets, which is described by Equation 1.6, the Cassie-Baxter equation.

This is a special case of the generic formulation for the contact angle on a heterogeneous surface comprised of distinct patches (Equation 1.4).[36] A liquid droplet floating in zero gravity in contact with air, affected only by surface tension forces, becomes a sphere, as this minimizes the surface free energy of the drop. Thus, the contact angle of any liquid on air is 180°, which may be substituted into the equation as $\cos 180° = -1$, to yield Equation 1.6.

The ϕ_s term is the areal fraction of the wetted solid, which is the projected area of the wetted patches divided by the projected area of the overall composite interface, and is always < 1. Each wetted patch is effectively in the Wenzel state, where r_ϕ is now strictly the Wenzel roughness of only the fraction of solid in contact with the liquid (Figure 1.4).

$$\cos\theta^* = \sum r_i \phi_i \cos\theta_i \tag{1.4}$$

$$\cos\theta^* = r_\phi \phi_s \cos\theta_E + (1 - \phi_s)\cos 180° \tag{1.5}$$

$$\cos\theta^* = r_\phi \phi_s \cos\theta_E + \phi_s - 1 \tag{1.6}$$

For a surface with given geometry, the minimum θ_E required to maintain a liquid in the Cassie state is readily calculated by equating the apparent contact angles given by equations 1.3 and 1.6, then solving for θ_E. This is represented on the θ^* vs. θ_E plot in Figure 1.5. This θ_E is termed the "critical contact angle", θ_c. The Cassie-Baxter state is only the global minimum-energy configuration when $\theta_E \geq \theta_c$. However, it is possible for meta-stable Cassie-Baxter states to exist even when $\theta_E < \theta_c$, as described in the following section.

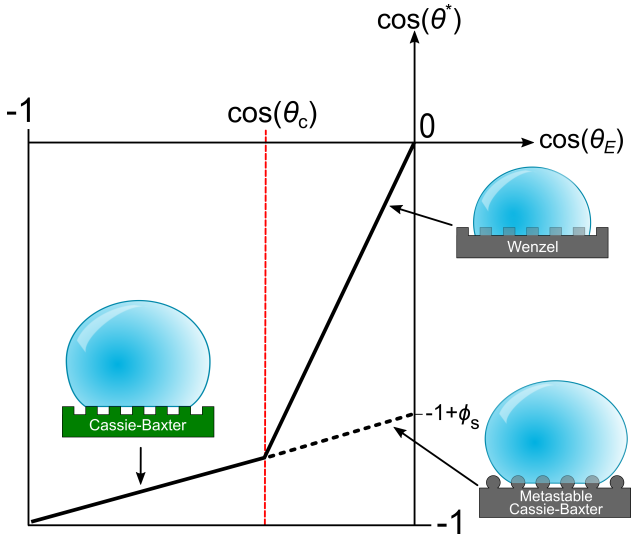

Figure 1.5: The transition between the Cassie-Baxter and Wenzel states on a given surface texture occurs when the Young's contact angle drops below a critical contact angle θ_c. Adapted from [37]

1.2.4 Repelling Low Surface Tension Liquids

Recall that low γ_{LV} liquids exhibit $\theta_E < 90°$ even on the lowest surface energy solid material, a perfluorinated monolayer. This means that a pillar array structure with smooth vertical sidewalls will never be able to suspend a low surface tension liquid in the Cassie-Baxter state, as the net surface tension force will point downward into the texture. However, it has been demonstrated that surfaces with overhanging, or "re-entrant", texture features can produce Cassie-Baxter states with low γ_{LV} liquids (Figure 1.6).[5,38–40] Since these liquids intrinsically wet the material used to fabricate these re-entrant structures, they necessarily exhibit a metastable Cassie-Baxter state (Figure 1.5).[41,42]

The re-entrance of a surface feature may be defined by the minimum texture angle, ψ_{min}. ψ is defined as 180° for a flat surface, 90° for a vertical wall, and 0° on the underside of a completely overhanging surface feature, such as a "microhoodoo", a pillar topped with a flat cap. As long as $\psi_{min} \leq \theta_E$ of the target liquid on the material of the surface, it may theoretically be suspended in the Cassie-Baxter state. It has been shown that so-called "doubly re-entrant", umbrella-like surface features with $\psi_{min} \approx -89°$, fabricated from un-modified silicon with very high surface energy can suspend even liquids with $\theta_E \approx 0°$, such as perfluorodecalin due to the texture alone, though with high $\Delta\theta$ due to the high wetted area of the flat circular caps.[43]

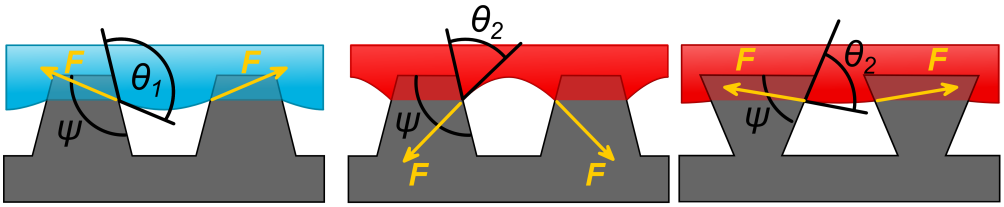

Figure 1.6: Liquids cannot be maintained in the Cassie-Baxter state unless the minimum texture angle ψ_{min} is less than the equilibrium contact angle of the liquid. Left: on a non- re-entrant surface with ($\psi_{min} \geq 90°$), it is possible to suspend a liquid with an equilibrium contact angle $90d \geq \theta_1 \leq \psi_{min}$. Middle: however, a second lower γ_{LV} liquid with $\theta_2 < 90°$ will spontaneously wet. Right: the same low-γ_{LV} liquid on a re-entrant texture with $\psi_{min} \leq \theta_2$ is now stable.

1.2.5 Robust Non-Wetted States

The breakthrough pressure (P_b) is defined as the applied pressure at which a given composite interface is disrupted by sagging of the liquid-vapor interface or displacement of the local contact line into the texture, causing a transition from the Cassie-Baxter state to the Wenzel state. For a given surface, P_b will vary depending on the properties of the contacting liquid. To isolate this effect, we use a non-dimensional robustness parameter, A^* which is given as follows:

$$A^* = \frac{P_b}{P_{ref}} \tag{1.7}$$

That is, the breakthrough pressure normalized by the minimum pressure applied by a millimetric scale droplet. This minimum pressure, P_{ref}, is determined by the properties of the liquid, as

$$P_{ref} = 2\gamma_{LV}\ell_{cap} \;=\; 2\gamma_{LV}\sqrt{\frac{\gamma_{LV}}{\rho}} \tag{1.8}$$

where γ_{LV} is the surface tension of the liquid, ℓ_{cap} is the capillary length, and ρ is the density of the liquid. An $A^* \gg 1$ indicates a robust composite interface, whereas an $A^* < 1$ indicates spontaneous wetting. A^* may be calculated for periodic geometries, such as arrays of pillars, microhoodoos, and cylindrical fibers.[40]

Naturally, larger diameter pores in a superhydrophobic or superomniphobic texture reduces the robustness of the Cassie-Baxter state. However, on a non-wetted surface with a simple periodic geometry, such as a pillar array, the only way to increase θ and decrease $\Delta\theta$, is to reduce ϕ_s, the solid-liquid contact area, by increasing the spacing of the texture elements. One may define D^*, the feature spacing ratio, or the inverse of ϕ_s, and rewrite the Cassie-Baxter equation (1.6) in terms of this parameter. The apparent contact angle θ^* increases with increasing D^*.

$$\cos\theta^* = \frac{1}{D^*}(r_\phi \cos\theta_E + 1) - 1 \tag{1.9}$$

The form of D^* depends on the geometry of the texture elements. For a square array of square-capped pillars or hoodoos,

$$D^* = \frac{(W + D)^2}{(W)^2} \tag{1.10}$$

where D is half of the edge-to-edge spacing, and W is half of the width of the square top. For a square array of circular-capped pillars or hoodoos,

$$D^* = \frac{4\,(R + D)^2}{\pi(R)^2} \tag{1.11}$$

where D is half of the edge-to-edge spacing, and R is the radius of the circular top. For parallel cylindrical fibers,

$$D^* = \frac{R + D}{R} \tag{1.12}$$

where D is half of the edge-to-edge spacing, and R is the radius of the fiber.

In all these cases, a trade-off arises between robustness and droplet mobility. However, a solution comes from the original inspiration for artificial superhydrophobic surfaces: the leaves of the lotus plant, *Nelumbo nucifera*, which exhibits both extremely high droplet mobility and high robustness. The leaves exhibit hierarchical structures, as is common in nature, formed from microscale bumps which are themselves covered in nanoscale crystals of hydrophobic wax. This second level of texture increases the effective D^* and therefore increases θ^* and decreases $\Delta\theta$, but without increasing the length scale of the largest pores.[44–46] This is schematically illustrated in Figure 1.7. The D^* of

hierarchical textures increases multiplicatively, *i.e.*,

$$D^*_{hierarchical} = \prod_{i=1}^{n} D^*_i \tag{1.13}$$

where n is the number of hierarchical levels. Extending the concept of hierarchical texture to multiple scales of re-entrant texture, *e.g.*, spherical microparticles on a mesh of cylindrical wires, also can yield extremely robust, low-$\Delta\theta$ Cassie-Baxter states with very low-γ_{LV} liquids.[47] This concept is also systematically explored in the work presented in Chapter 2.

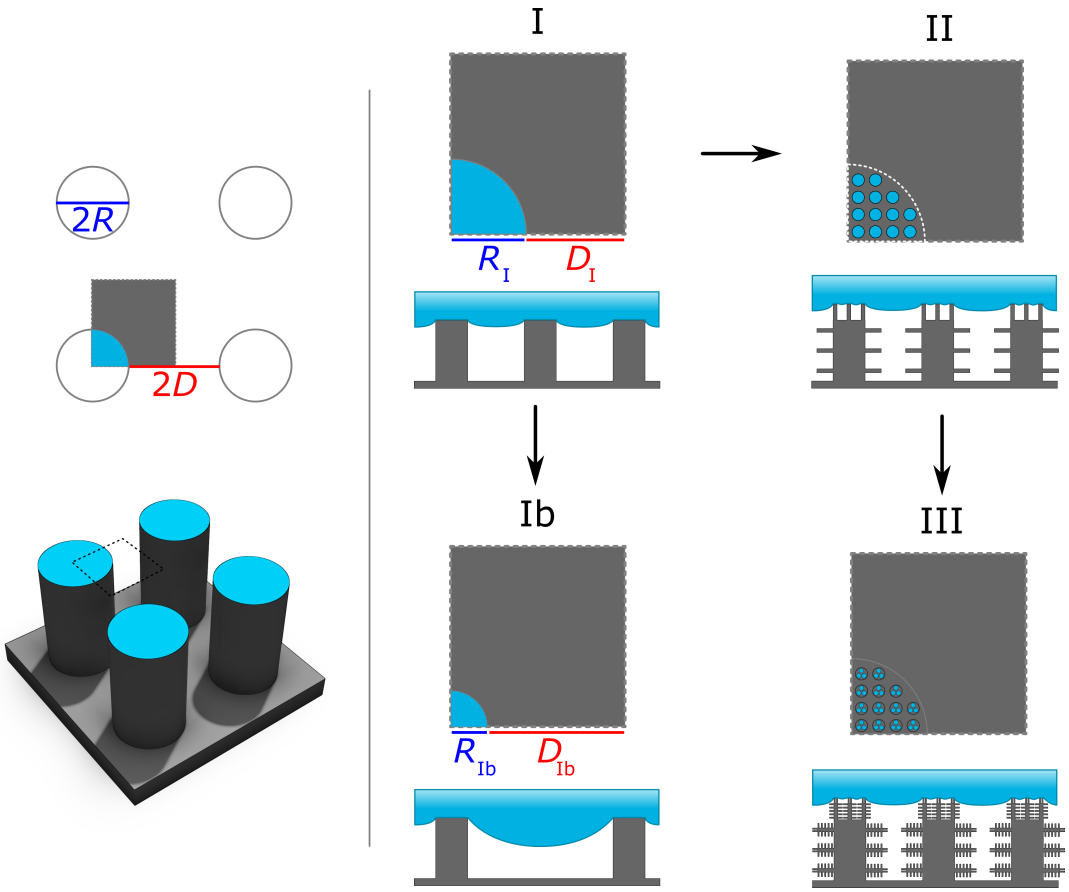

Figure 1.7: While increasing the spacing ratio D^* of a single-level texture (*I* to *Ib*) increases liquid repellence only by compromising the non-wetted state robustness, adding hierarchical texture elements can achieve both aims. Repeatedly covering the original pillar array with smaller pillars (*II*, *III*) dramatically reduces the area wetted by the liquid, marked in blue, while maintaining the largest effective pore size D_I, and therefore also the breakthrough pressure, of the original array.

1.2.5.1 Measurement of Breakthrough Pressure

Resistance to wetting under pressure may be experimentally measured by various methods, including immersion in a column of liquid, impacting droplets from varying heights, or measurement with drops with very small volumes and high curvatures.[48] The hydrostatic pressure applied by a column

of liquid is readily calculated as

$$P = \rho g h \tag{1.14}$$

where ρ is the density of the liquid, g is the acceleration due to gravity, and h is the height of the liquid above the sample. The wetting state on an immersed textured surface is frequently difficult to observe, as not all textures will exhibit an evident reflective layer of air, or "plastron". Droplet impact is frequently used as an alternative, as there is a clear transition between a droplet rebounding in the Cassie-Baxter state, or remaining pinned in the Wenzel state. However, the exact applied pressure of a droplet impacting from a height h is more complex. The lower bound is the dynamic pressure in equation 1.15, as

$$P = \frac{1}{2}\rho V^2 \tag{1.15}$$

where ρ is the density of the liquid and V is the impact velocity. However, the instantaneous pressure has been claimed to be higher due to shockwaves propagating in the droplet. One such estimate is referred to as the water hammer pressure,[49,50] which may be calculated as

$$P = k\rho C V \tag{1.16}$$

where k is a constant determined by the impact geometry, and is typically taken to be 0.2 for a spherical droplet impacting a planar surface, ρ is the density of the liquid, C is the velocity of sound in the liquid, and V is the velocity of the droplet. In our work, however, the droplet impact pressure was assumed to be equivalent to that in Equation 1.15, as a conservative estimate.

Contact angle measurements with small droplets may also be used to measure wetting under elevated pressures. A curved liquid meniscus generates a pressure due to the surface tension, known as the Laplace pressure. This is given by

$$P = 2\frac{\gamma_{LV}}{R} \tag{1.17}$$

where γ_{LV} is the surface tension of the liquid and R is the radius of curvature of the interface. Spherical drops of decreasing volume therefore exhibit increasing Laplace pressures, and this is a relatively convenient and controlled method to apply higher pressures. However, this method may not be well-defined when the drop diameter approaches the length scale of the textured surface geometry, and the assumptions of the wetting state equations of a randomly textured, homogeneous surface no longer hold. Additionally, the exact pressure when the droplet begins to wet and no longer adopts a spherical geometry is poorly defined.

1.2.6 Terminology for Describing Wettability

The response of a liquid on a surface is conventionally categorized as "phobic" or "philic" in terms of static contact angle, as in Figure 1.2. This highlights whether or not a liquid spontaneously wets a surface or beads up. This definition, however, is incomplete for describing the suitability of surfaces with engineered wettability for many applications, as it ignores the mobility of liquid droplets on the

surface. While increasing droplet mobility is generally correlated with increasing contact angle, particularly with the onset of the Cassie-Baxter state, many exceptions exist. Surfaces with very high θ_E ($> 150°$) may also exhibit $\theta_r^* \approx 0°$, resulting in droplets which are completely adhered to the surface despite entrapped air pockets. This may or may not be a desirable behavior. Such surfaces should clearly not be deemed "superhydrophobic" with no qualifiers simply because the $\theta_E > 150°$. Conversely, there are a growing number of smooth surfaces that are capable of readily shedding low-γ_{LV} liquids, but with $\theta_E < 90°$, and are commonly referred to as "omniphobic".[8,51] Alternatively, Cheng, *et al.* referred to their surface exhibiting low $\Delta\theta$ with linear alkanes as "statically oleophilic" but "dynamically oleophobic", which is less concise but perhaps more precise.[52] The conventions in the literature are therefore not always consistent, and a meaningful presentation of a surface with engineered wettability must include dynamic contact angle data to accurately convey information.[25,26] Table 1.3 contains some of the commonly used nomenclature in literature and examples of surfaces which fall into these categories. Throughout this thesis, we report dynamic contact angles, or at least the closely-related droplet sliding or roll-off angles, to avoid ambiguity where possible.

1.3 Overview of Research

The design and optimization of SHSs/SOSs fabricated by a diverse array of methods has been well studied.[1–6,40,57,62–69] However, most natural and artificial SHSs/SOSs suffer from poor mechanical durability, including the hierarchically structured hyperbranched surfaces reported in Chapter 2; their surface features typically are so fragile that they can be easily removed even by the swipe of a finger.[65] There are limited reports of SHSs/SOSs demonstrated to survive the harsh conditions experienced in a wide array of engineering applications. Chapter 3 details the development of several mechanically robust, scalable superhydrophobic spray-coatings. The optimal porous but coalesced texture was found to form due to the partial phase separation of low-γ_{SV} fillers from resilient polymer matrices. Such blends were systematically identified using Hansen Solubility Theory. The superhydrophobicity of these surfaces was retained after significant abrasion damage under an industry-standard rotary abrasion test, and could be recovered by heating after damage from numerous other chemically and physically damaging exposures. However, the surface feature length scale of these surfaces were primarily in the tens to hundreds of micrometers, which limited their resistance to wetting under high pressures, their transparency, and their ability to reduce drag in turbulent flows. These issues are partly addressed with the addition of hierarchical nanostructure to these surfaces and the reduction of their overall roughness, as discussed in Section 3.7.

Additionally, wetting due to applied pressure is exacerbated by low liquid surface tension. It is possible to modify the durable spray-coatings to produce superomniphobic surfaces capable of repelling some low-γ_{LV} liquids, but not without compromising their mechanical robustness (see

Table 1.3: Some possible liquid wettabilities, organized generally from wettable to non-wettable. Water is distinct from all other liquids because of its anomalously high γ_{LV} and high polarity. Oils tend to be non-polar, moderate surface tension liquids such as medium chain alkanes, *e.g.*, hexadecane. "Omni-" includes much lower γ_{LV} liquids such as polar solvents, silicone oil, and fluorinated liquids, but not necessarily simultaneously. Adapted from the dissertation of Kevin Golovin.

Designation	Repels	θ (°)	$\Delta\theta$ (°)	Examples
Superomniphilic	None	$\theta_E \approx 0°$	–	Ultra-clean smooth polar solids (oxides, metals). Roughened high surface energy solids, *e.g.*, paper.
Superoleophilic	Water	$\theta_E \approx 0°$	–	Roughened intermediate surface-energy polymers exhibit intermediate contact angles with water but wet with oil.
Hydrophilic-Oleophobic	Oils but not water	$\theta_E \gg 0°$	–	Counter-intuitive surfaces with responsive functional groups capable of selectively wetting with polar liquids and repelling non-polar ones with lower γ_{LV}, *e.g.*, fluoro-compounds embedded in hydrogels or tethered fluorosurfactants.[4,53]
Hydrophobic	Water	$\theta_E > 90°$	–	Smooth polyethylene.[54] Also tend to be oleophilic.
Sticky superhydrophobic	Water	$\theta^* > 150°$	$\Delta\theta^* \gg 10°$ †	Superhydrophobic surfaces with (deliberately) introduced wetting defects. Tend to be superoleophilic.[55]
Superhydrophobic	Water	$\theta^* > 150°$	$\Delta\theta^* \approx 0°$	Several leaves, including the lotus.[56] Also tend to be (super)oleophilic.
Oleophobic	Oils	$90° < \theta^* \ll 150°$	–	Roughened PTFE[1]
Superoleophobic	Oils	$\theta^* > 150°$	$\Delta\theta^* < 10°$ †	Micro-hoodoos, electrospun systems.[40] Some authors prefer "superamphiphobic"[57,58]
Omniphobic	All	–	$\Delta\theta^* \approx 0°$	Perfluorinated lubricated surfaces, grafted liquid-like films, and smooth perfluorinated films.[8,51,59]
Superomniphobic	All	$\theta^* > 150°$	$\Delta\theta^* < 10°$ †	Hierarchcial perfluorinated re-entrant texture[47,60,61]

†No broad consensus in the surface science community.

Section 4.2.2 and Figure 4.11). In Chapter 4, we demonstrate smooth, all-solid, and substrate-independent coatings produced from the similar materials to the durable superhydrophobic surface described above, also optimized for partial miscibility. These coatings exhibited low sliding angles with liquids with broadly varying γ_{LV}, from water to silicone oil, were invulnerable to wetting under impact, and were transparent. This approach addressed drawbacks inherent to lubricated systems and molecular monolayer approaches mentioned above. Lubricated surfaces can result in relatively pressure-stable repellency to a broad range of liquids immiscible with the infused inert liquid, but the addition of a liquid component to the system compromises mechanical durability and long term retention of non-wetting properties. Covering a substrate with self-assembled monolayers of low surface energy molecules also requires careful processing and is highly dependent on matching surface chemistry with the reactive molecule to achieve smooth, uniform coverage. The coatings described here may be applied with simple methods to a broad range of materials to render them omniphobic.

However, these smooth coatings remained vulnerable to elevated temperatures, and abrasion resistance was only moderately improved compared to textured superomniphobic or lubricated surfaces. They also could not repel solvents that strongly swelled the matrix polymer or dissolved the fluorinated filler. In subsequent work, presented in Chapter 5, it was found that a grafted layer of poly(dimethyl siloxane) on silicon and glass substrates achieved similarly low $\Delta\theta$ with a broad range of liquids, even ultra-low-γ_{LV} fluorinated lubricants. This surface treatment was found to be comparatively invulnerable to elevated temperatures and light abrasion. The ultrathin liquid-like layers also reduced adhesion to various solid contaminants, as well as permitted the easy removal of films of marine algae.

Additionally, liquid-repellent surfaces may be spatially patterned to confine liquids into domains or channels. This has applications in open-channel microfluidic devices, which have the potential to be much less expensive and easier to fabricate than their closed-channel counterparts. This is especially true when they are produced on inexpensive substrates such as fluorinated paper, with wettable channels deposited using simple printing methods. The work in Chapters 6, 7, and 8 focused on extending the capability of open-channel microfluidic devices to contain low-γ_{LV} liquids, enabling a number of applications thus far unexplored on open-channel devices.

The final chapter reports another application of robust, hierarchically textured superhydrophobic surfaces: culture plates capable of readily generating free-floating spheroidal clusters of cancer cells for *in vitro* biological studies and therapeutic assays which have improved accuracy over conventional two-dimensional culturing methods. Compared to commonly used hanging drop plates, which suspend droplets from hydrophobic surfaces, these superhydrophobic plates are significantly more resistant to droplet loss due to impact during routine handling.

CHAPTER 2

Rational Design of Hyperbranched Nanowire Systems for Tunable Superomniphobic Surfaces Enabled by Atomic Layer Deposition

This chapter is paraphrased from a published article in *ACS Nano*,[61] and was a collaborative effort with Prof. Neil Dasgupta. The fabrication method was primarily developed by Ashley Bielinski, who is an equal first author on the manuscript. It is included here as a systematic experimental demonstration of some of the wettability parameters outlined in Section 1.2.

2.1 Introduction

As discussed in the introductory chapter, superomniphobic surfaces display contact angles $\theta^* > 150°$ and low contact angle hysteresis with virtually all high and low surface tension liquids, including water, oils, solvents, acids, bases, and alcohols. Over the last decade, such surfaces have attracted immense commercial and academic interest due to their potential to impact a large number of applications such as self-cleaning surfaces,[70] non-fouling surfaces,[71] stain-free clothing and chemical-resistant protective wear,[72] drag reduction,[73] corrosion prevention,[74] and separation of liquids.[75] Previous work has discussed the significance of surface energy, roughness, and the critical role of re-entrant texture in obtaining surfaces that can repel low surface tension liquids such as oils, solvents and alcohols.[5,39,42] Previous work has also discussed how hierarchical scales of texture (*i.e.*, texture on two or more length scales) can yield high contact angles and decrease the contact angle hysteresis of superomniphobic surfaces by reducing the solid-liquid contact area.[46,47,76]

Here, we report a method for the systematic design and fabrication of hierarchical zinc oxide nanowire structures which may be tuned to selectively repel liquids of various surface tensions. This is enabled by independent tuning of the geometric parameters at each hierarchical level.[77] Figure 2.1 describes the three levels of branched hierarchy, along with the nanowire spacing, size, and orientation design parameters that are manipulated at each level (D_x, R_x, and θ_x, respectively, where x indicates the level of hierarchy). Branched NWs with tunable density and orientation were grown via a sequential hydrothermal process, in which atomic layer deposition (ALD) was used for

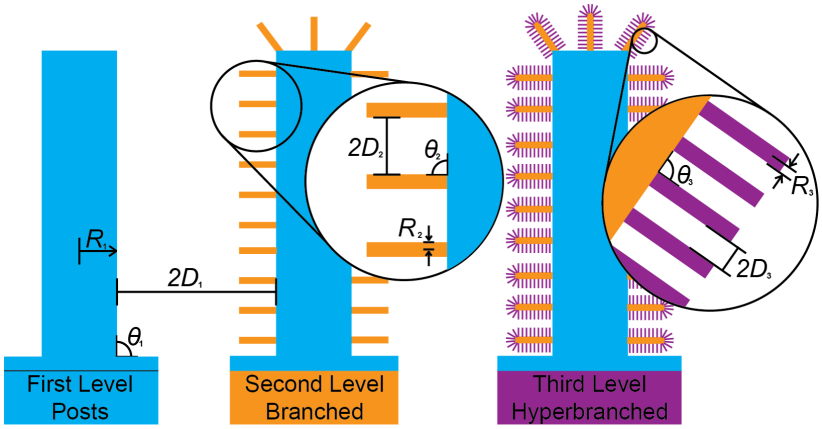

Figure 2.1: Diagram showing three successive levels of hierarchy along with the size, density, and orientation design parameters that can be controlled at each level.

NW seeding, disruption of epitaxy, and selective blocking of NW nucleation. This approach allows for the rational design and optimization of three-level hierarchical structures, in which the geometric parameters of each level of hierarchy can be individually controlled. We demonstrate the coupled relationships between geometry and contact angles for a variety of liquids, which is supported by mathematical models. The most repellent superomniphobic surface was designed with three levels of hierarchy and achieved the following advancing/receding contact angles with water: 172°/170°, hexadecane: 166°/156°, octane: 162°/145°, and heptane: 160°/130° (Table 2.1).

Prior to this work, it had not been possible to fabricate superomniphobic surfaces with three or more hierarchical scales of texture where the size, spacing, and angular orientation of features within each scale of texture can be independently varied and rationally controlled. This capability would enable the systematic study of the parameters that affect the robustness of superomniphobicity.[78,79] Achieving such independent control over the geometry requires new approaches that overcome the limitations of conventional top-down lithographic processes. Most current approaches to the assembly of hierarchical NW structures onto a substrate begin with either a patterning step such as lithography or self-assembly, or rely on stochastic processes such as random attachment or supersaturated phase transformations.[80–86] Patterning steps are limited by resolution, scalability, substrate compatibility, and cost. In particular, challenges arise when non-planar substrates are used, as photolithography is line-of-sight limited. Random attachment or supersaturation methods are simple and low-cost, but they lack the control over the feature size, orientation, and spacing needed to enable materials by design. While complex hierarchically-branched nanostructures can be formed using a variety of colloidal synthesis approaches,[87–89] the formation of ordered assemblies spanning multiple length scales and over large area substrates remains challenging using solution-phase chemistry alone. In particular, the ability to produce tunable 3D features on the surface of high aspect ratio substrates requires extremely conformal deposition processes, as each sequential level

of hierarchy must be assembled on the previous nonplanar surface.

For bottom-up NW growth, directed heterogeneous nucleation on nonplanar substrates requires control over the substrate surface chemistry and crystallographic texture. The rational growth of branched and hyperbranched NWs has been previously demonstrated using sequential seeding processes that rely on either solution- or vapor-phase deposition (typically sputtering or evaporation) of catalyst seeds onto NW surfaces.[90–94]

However, these approaches are limited in their ability to simultaneously control seed size, density and crystallographic orientation, especially over high-aspect ratio surfaces with both concave and convex features. This becomes increasingly challenging with multiple levels of hierarchy. Additionally, the use of high temperature and/or high vacuum processes limits the scalability and substrate compatibility of these approaches. To overcome this limitation, we used atomic layer deposition (ALD) to independently control the interfacial composition, morphology, and microstructure of seed layers between three different levels of hierarchy, which directed subsequent heterogeneous nucleation and growth of hyperbranched structures.

2.2 Rational Design of Superomniphobic Surfaces

Superomniphobic rough surfaces featuring hierarchical scales of texture are critical for achieving very high contact angles while maintaining a stable and robust composite interface with low surface tension liquids. The porosity of the largest texture scale determines the robustness of the Cassie-Baxter state, or its resistance to liquid impingement under pressure. As a consequence, adding multiple levels of texture reduces the solid-liquid contact area, ϕ_s, without compromising the surface's robustness against wetting.[47,77,95] We have previously shown that re-entrant or overhanging texture is also critical for enabling the Cassie-Baxter state with low surface tension liquids, such as oils and organic solvents, for which the Young's contact angle is $\theta \ll 90°$.[5,6,74] The nanowire growth method demonstrated in this work is ideally suited to fabricating surfaces with multi-level hierarchical scales of re-entrant texture.

Ideally, achieving a composite interface with a low ϕ_s also minimizes contact angle hysteresis, $\Delta\theta$, or the difference observed between the maximum or advancing contact angle (θ_a^*) and the minimum or receding contact angle (θ_r^*) measurable on different surfaces. This is because any contacting liquid has effectively no interaction with the entrapped air. Surfaces with minimal $\Delta\theta$ allow liquid droplets to easily roll or even bounce off.[47,77,95] Our capability of adding multiple levels of branched nanowires, as illustrated in Figure 2.1, has the potential to significantly reduce ϕ_s, increase θ^* and decrease $\Delta\theta$ simultaneously without increasing the largest length scale of porosity, which would compromise the robustness of the composite interface. By controlling the individual geometric parameters of each level of hierarchical texture in this study, we demonstrate that model-based design of materials with tunable contact angles, contact angle hysteresis, and Cassie-Baxter state

robustness is feasible. Overall, this new technique could prove to be a powerful platform for the systematic design of superomniphobic structures.

2.3 Materials and Methods

2.3.1 Atomic Layer Deposition

Atomic Layer Deposition (ALD) is a vapor-phase thin film deposition process based on sequential exposure of a substrate to precursors that undergo self-limiting surface reactions.[96] The precursor sequence can be altered over the course of film deposition to create laminar structures or compositional variations with sub-nanometer resolution.[97] The deposition process is not line-of-sight limited, enabling conformal coverage of ultra-high aspect ratio (>2000:1) structures with negligible thickness variation.[98] We demonstrate here the power of ALD to control the hydrothermal synthesis of hyperbranched nanostructures on non-planar surfaces. The atomic scale control of thickness, position, and crystal structure provided by ALD enables independently programmable control of feature size, density, and orientation within each level of the hierarchical structure, as shown in Figure 2.1. Furthermore, this low-temperature approach can be scaled to a wide range of substrates, including flexible plastics and paper.[99] The details of the ALD apparatus used may be found in previously published articles from the Dasgupta group.[93,99]

2.3.2 Substrates, Seed Layer, and Dense Unbranched Nanowires

The hierarchical nanostructure synthesis procedure starts with the hydrothermal growth of ZnO NWs on planar silicon wafers or arrays of cylindrical microposts. The microposts were fabricated via conventional photolithographic techniques in the Lurie Nanofabrication Facility. Clean silicon wafers were spin coated with a 3 μm layer of Dow Megaposit SPR 220 photoresist, which was patterned into arrays of circular dots. The patterned surface was then anisotropically etched using a conventional Bosch Deep Reactive Ion Etch (DRIE) process in an STS Pegasus 4, which involves alternating cycles of plasma etching and passivation. ALD ZnO films were deposited onto substrates as a nanocrystalline seed layer to promote heterogeneous nucleation. It was deposited at a substrate temperature of 150 °C using diethyl zinc and DI water as the precursors, resulting in a polycrystalline wurtzite film which increased in thickness at 2.0Å/cycle. Grains in the seed layer with crystallographic orientation provide thermodynamically favorable nucleation sites for ZnO NWs.[100] The final dimensions of the pillar arrays are noted in Table 2.1 and an example is shown in Figure 2.2.

After the seed layer was deposited, the NWs were grown using a low temperature, atmospheric pressure hydrothermal growth procedure, which has been previously published.[99,100] The samples were immersed in a solution of zinc nitrate hexahydrate (25 mM), hexamethylenetetramine (25 mM), and polyethylenimine (5 mM) in DI water. The hydrothermal growth was performed at 90 °C and

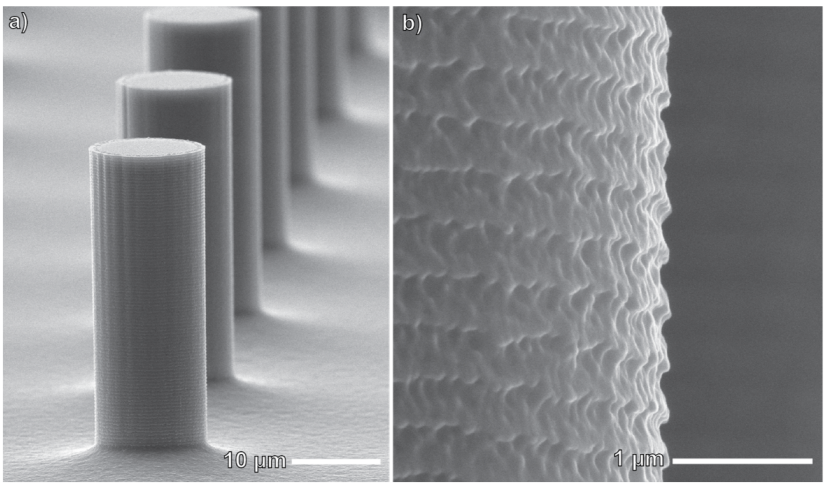

Figure 2.2: (*a,b*) SEM images showing silicon micropost arrays with a smooth, highly conformal seed layer of ZnO deposited by ALD. The scalloped side walls from the cyclic Bosch etch process can be clearly seen.

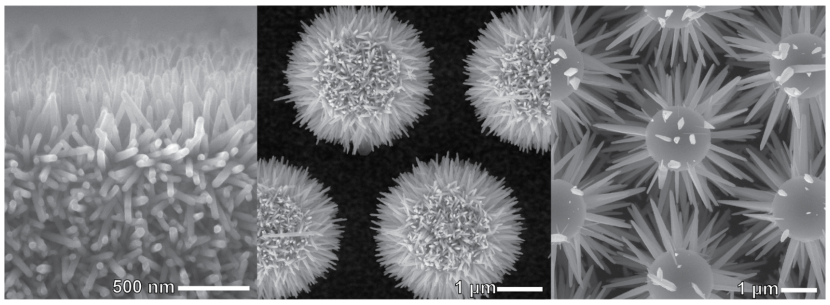

Figure 2.3: SEM images of silicon microposts with ZnO nanowires.

ambient pressure for 30 to 90 minutes. Varying time yielded varying lengths of nanowires. The substrates were suspended facing at a downward angle in the solution to prevent homogeneously nucleated precipitate from settling on the surface.

We have previously shown that properties of the ALD seed layer, including grain orientation, roughness, and surface stress effects, can be precisely tuned, allowing for rational control of the resulting NW array properties such as axial orientation, density, and size. Control of NW growth is possible regardless of the starting substrate material or geometry, including hierarchical growth on high-aspect ratio surfaces. Figure 2.3 shows examples of single nanowires of varying size on silicon microposts.

2.3.3 Perpendicular Nanowires with Tunable Spacing

Hierarchical structures require the sequential growth of branched NWs with independent control of size, orientation, and spacing. This necessitates that the initial "trunk" nanowires are sufficiently spaced (D_2 in Figure 2.1) as well as perpendicularly oriented to the substrate ($\theta_2 = 90°$) to allow subsequent branches to fit. We developed a new ALD seeding technique that decoupled the NW orientation and density, unlike in our previous work.[99] As shown in Figure 2.4a, ALD was used

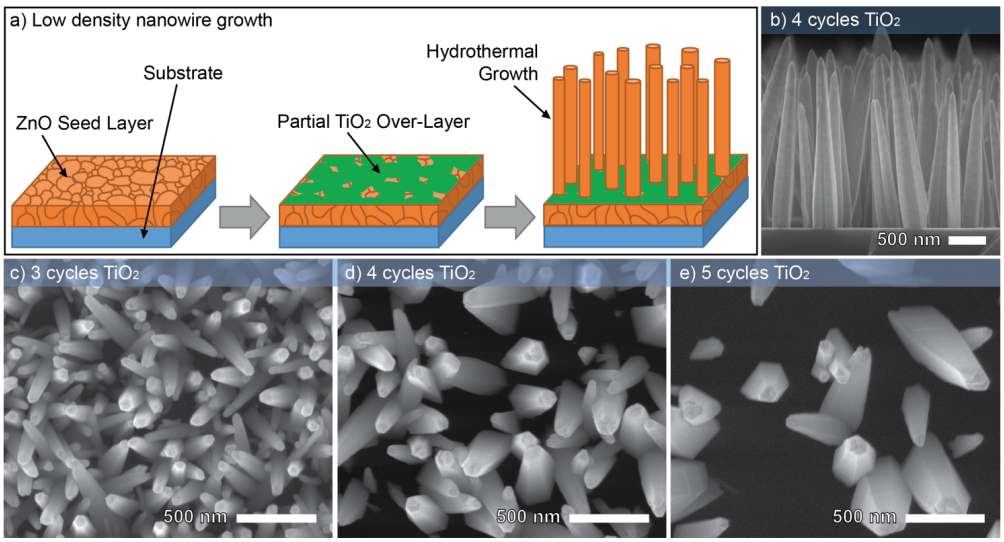

Figure 2.4: (*a*) Diagram of the low-density NW growth procedure showing the ZnO seed layer, partial TiO_2 overlayer, and hydrothermal NW growth. (*b*) 90° cross-section SEM image of low-density NWs grown with 4 cycles of TiO_2 over a 100 cycle ZnO seed layer showing NW orientation perpendicular to the substrate. (*c–e*) top-down SEM images of NWs grown with 3, 4, and 5 cycles of TiO_2 over a 100 cycle ZnO seed layer showing decreased array density, increased D_2 values, with increased number of TiO_2 cycles. The increase in diameter observed with the decrease in density is a result of decreased steric hindrance and decreased mass transport limitations in the growth solution at the base and sides of the nanowires.

to first deposit a ZnO seed layer with preferential texture to enable perpendicular NWs. Then, a second incomplete monolayer was deposited on top of the ZnO seed layer consisting of 3–5 cycles of amorphous ALD TiO_2, which does not seed ZnO NW growth. It was deposited at a substrate temperature of 200 °C using tetrakis(dimethylamido)titanium and DI water as the precursors, resulting in an amorphous film that grew in thickness at 0.6 Å /cycle. Thus, the incomplete TiO_2 layer partially blocks nucleation sites on the ZnO seed layer, while still leaving some exposed crystalline regions to the growth solution. Due to the self-limiting nature of ALD, the surface fraction of the seed layer that is masked from the solution can be precisely and reproducibly controlled with sub-monolayer precision by varying the number of ALD TiO_2 overlayer cycles.

Figures 2.4c–e shows the progressive decrease in NW density as the number of TiO_2 overlayer cycles is increased from 3 to 5. This can be accomplished irrespective of substrate material and geometry, by simply "encoding" the recipe for NW growth in the ALD seed layer. This enables independent control of inter-NW spacing, D_2, as determined by the TiO_2 partial interlayer, while maintaining perpendicular orientation, $\theta = \sim 90°$, which is determined by the ZnO seed layer, shown in Figure 2.4b. When using thinner TiO_2 overlayers (1–2 cycles), the NW density remains nearly identical to that on the initial seed layer, suggesting insufficient blocking of active sites for heterogeneous nucleation. For thicker overlayers of ≥ 6 cycles, the NW density continues to decrease until a continuous TiO_2 overlayer forms, at which point the density is effectively zero.

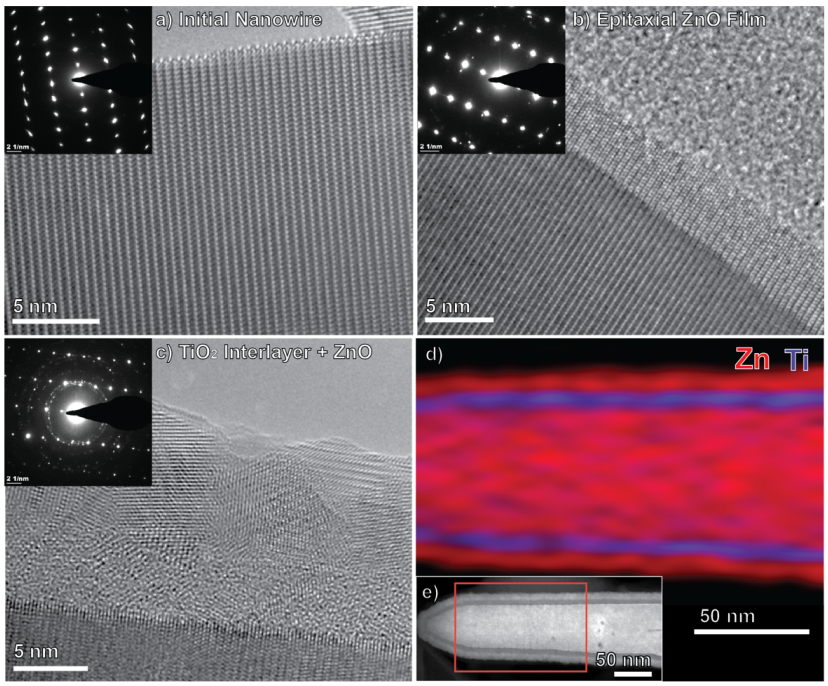

Figure 2.5: HRTEM and annular diffraction patterns (inset) of (*a*) single-crystalline ZnO NW, (*b*) ZnO NW with epitaxial ALD ZnO film growth, and (*c*) ZnO NW with amorphous ALD TiO_2 blocking layer and polycrystalline ALD ZnO seed layer. (*d*) EDX analysis for element mapping, and (*e*) dark field STEM image of ZnO NW with ALD TiO_2 and ZnO films, where the red box shows the area analyzed in (*d*).

2.3.4 Branched Nanowires

Sequential deposition of a ZnO seed layer on uncoated ZnO nanowires was not successful, as epitaxial growth was observed despite the low temperature (150 °C) used, thereby merely enlarging the initial NWs. The epitaxial growth behavior was confirmed using high-resolution transmission electron microscopy (HRTEM), shown in Figure 2.5. NW arrays were grown on planar silicon substrates, coated with the desired ALD films, and then transferred to TEM grids for study. Three samples were observed. The first was a control sample of as-grown ZnO NWs. The second had a shell of 50 cycles of ZnO deposited on the ZnO NWs, and the third had an inner shell of 100 cycles of TiO_2 followed by an outer shell of 50 cycles of ZnO.

In order to block epitaxial growth, we devised a method to deposit an interlayer between the initial low-density NW array and the second ZnO seed layer for the branches as shown in Figure 2.6a. For this, we used thin (50–100 cycle) ALD TiO_2 interlayers. Unlike the incomplete TiO_2 films used for the low-density synthesis, > 50 cycles of TiO_2 creates a complete film that totally encapsulates the surface, creating a core-shell structure. Figure 2.5c shows that the addition of an amorphous TiO_2 interlayer between the core NW and ALD ZnO layer disrupts epitaxial growth, resulting in a nanocrystalline ZnO outer shell. This ability to synthesize coaxial core-shell-shell NWs with programmable thickness, composition, and crystallinity is uniquely enabled by the ALD process.[93]

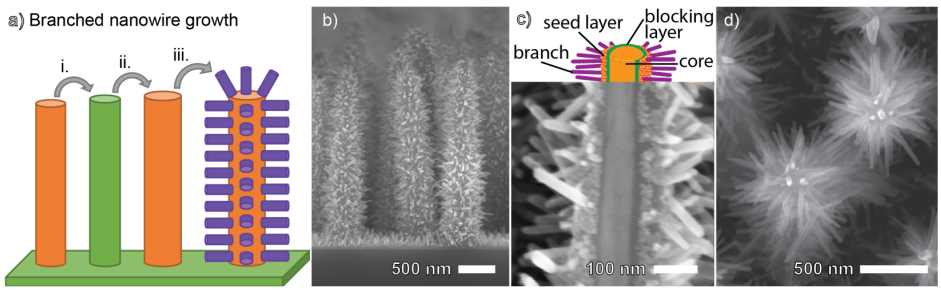

Figure 2.6: (*a*) Diagram of ALD interlayer procedure for branched NW seeding, starting with an array of low-density ZnO NWs, then adding: (*i*) ALD TiO_2 blocking layer, (*ii*) ALD ZnO seed layer, then (*iii*) Hydrothermally grown NWs. (*b*) Cross-section SEM of branched ZnO NWs. (*c*) Cross-section SEM and diagram of a split branched NW and showing the NW core, ALD TiO_2 blocking layer, ALD ZnO seed layer, and ZnO branches. (*d*) Top-down SEM of branched ZnO NWs.

Figure 2.5d shows EDX elemental mapping for the boxed region of the ZnO NW with coaxial TiO_2-ZnO shell imaged in the lower magnification dark-field STEM image in Figure 2.5e. This elemental map shows that the ALD films coat the NW conformally and that the shell interfaces remain distinct. For the TEM samples, 100 cycles (6 nm) of TiO_2 was used for the blocking layer as it was easier to image than the 3 nm film used in the standard synthesis procedure.

2.3.5 Hierarchical Structures

The two strategies detailed above: partial blocking of the ZnO seed layer, and blocking of epitaxial growth, may be combined to fabricate highly hierarchical structures with independently tunable parameters (Figure 2.6). The thickness of the partial blocking TiO_2 layer controls "trunk" nanowire geometry (R_2, D_2, and θ_2), and the number of cycles of the second epitaxially-blocked ZnO seed layer controls the "branch" geometry (R_3, D_3, and θ_3). SEM images of branched ZnO NWs with large inter-trunk spacing is shown in Figure 2.6b. Figure 2.6c shows a cross-sectional SEM image of a single branched NW that fractured along its axis, in which the core NW, amorphous TiO_2 blocking layer, nanocrystalline ZnO shell seed layer, and ZnO branches can all be clearly resolved.

Figure 2.7 shows SEM images of branched NWs grown perpendicular to the surface of silicon microposts. The SEM images demonstrate that the synthesis method described above for branched NWs with controlled density is suitable for growth on textured substrates with high aspect-ratios, and is not line-of-sight dependent. These posts were synthesized using standard photolithography and anisotropic dry etching for simplicity, however, the substrate versatility of this approach allows for conformal coating of virtually any micro- or nano-structured surface fabricated from various materials. Figures 2.7b,c shows that the control of NW size, orientation, and inter-NW density can be independently controlled and maintained along the entire surface of these textured structures. For example, by increasing the number of ALD TiO_2 overlayer cycles before the ZnO NW "trunk" layer growth, Figure 2.7c demonstrates that a larger inter-NW spacing of the trunks can be conformally

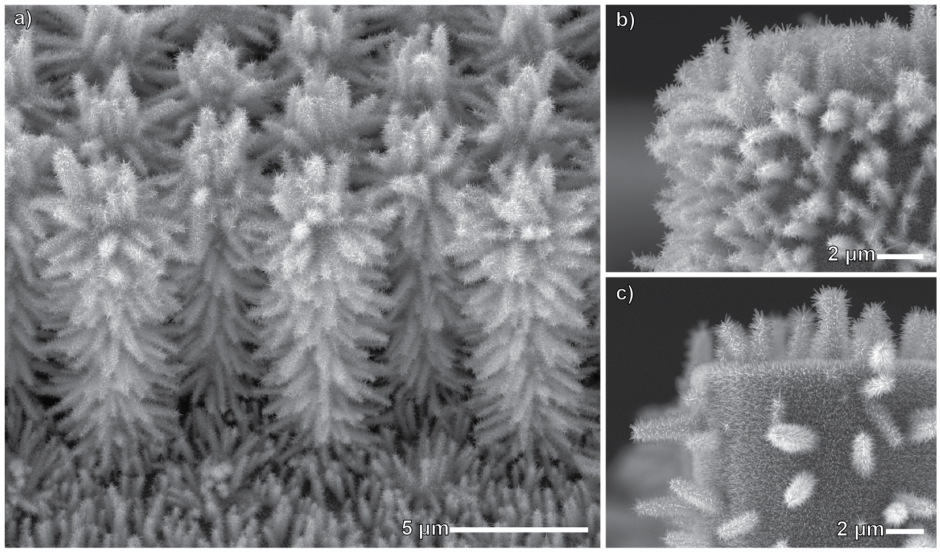

Figure 2.7: SEM images of various hyperbranched structures with three levels of hierarchy (*a*) 45° view of branched ZnO NWs on silicon microposts (seeded by a 4 cycle TiO_2 overlayer), (*b*) branched NWs grown with higher density "trunks" (seeded by a 4 cycle TiO_2 overlayer) (*c*) branched NWs grown with lower density "trunks" (seeded by a 5 cycle TiO_2 overlayer).

achieved along the micropost surface. The resulting hyperbranched structures thus allow for individual control of each level of hierarchy in this three-level structure, as proposed in Figure 2.1, enabling the design and optimization of surface texture for structural omniphobicity, which is described in the following section.

2.3.6 Fluoro-silanization

A low-surface-energy coating is necessary to render the hierarchical structures non-wettable by most liquids. The lowest surface energy material is a trifluoromethyl monolayer, so a fluorinated silane was chosen as the modifying layer. A final overlayer of 50 cycles of Al_2O_3 was deposited on each sample to prepare the surface for silanization, as silanes react best with hydroxyl-rich oxide surfaces such as Al_2O_3, SiO_2, and TiO_2. Al_2O_3 was deposited at a substrate temperature of 150 °C using trimethylaluminum and DI water as the precursors. The Al_2O_3 was amorphous as-deposited and had a growth rate of 1.0Å/cycle. The samples were then cleaned and activated with oxygen plasma for 30 minutes (30W, Harrick Plasma PDC-001). A simple vapor-phase silanization was carried out by covering the sample on a 125 °C hot plate next to a cuvette of (heptadecafluoro-1,1,2,2-tetrahydrodecyl)-1-trichlorosilane for 2 hours. The samples were then rinsed with 2,3-dihydrodecafluoropentane (Dupont Vertrel XF) and isopropyl alcohol (Fisher Scientific) and dried with compressed air prior to measurement.

2.3.7 Characterization Methods

2.3.7.1 Electron Microscopy

A TESCAN Mira 3 scanning electron microscope was used for the SEM images. The TEM images, STEM image, and EDS analysis were performed using an FEI Titan 80-300 transmission electron microscope, which was operated at 300 kV and fitted with a spherical aberration corrector for the objective lens.

2.3.7.2 Contact Angle Measurements

Contact angle measurements were performed with a Ramé-Hart 200-F1 contact angle goniometer using the sessile drop technique, as described in Section 1.2.2. Deionized water, as well as hexadecane, decane, octane, hexane, and heptane (purchased from Fisher Scientific) were used as probe liquids. Advancing and receding contact angles were obtained by measuring the angle while the liquid was slowly added to or removed from a ~3 μL droplet in contact with the sample and a micrometer syringe. At least three measurements were performed per sample and the standard error was $\pm 2^{\circ}$.

2.3.7.3 Breakthrough Pressure Measurement

Droplets of hexadecane were released from a measured height above the sample from a micro-syringe. The droplet impact was recorded with a high-speed camera (Fastec Imaging HiSpec 1). Droplets that did not rebound completely were considered to have exceeded the breakthrough pressure and partially wetted the texture. As discussed in the introductory chapter, the minimum pressure exerted by an impinging droplet released from a height h may be estimated by Equation 1.15. The highest pressure at which droplets completely rebounded was normalized with P_{ref} to yield an experimentally measured robustness parameter A^* for hexadecane on each surface.

2.4 Results

To demonstrate the application of these structures as a platform for systematically designing superomniphobic surfaces, we performed a series of experiments to establish the relationship between hierarchical scales of texture and liquid repellency. In all cases, the outer surface of structures was modified by surface functionalization with a perfluorinated monolayer (see methods). This allowed for a consistent surface energy for all of the fabricated samples, enabling quantitative comparison of purely geometric effects on the obtained contact angles. On smooth planar samples, this perfluorinated monolayer treatment yielded advancing and receding contact angles with water, hexadecane, octane, and heptane of $117^{\circ}/92^{\circ}$, $67^{\circ}/54^{\circ}$, $51^{\circ}/41^{\circ}$, and $43^{\circ}/39^{\circ}$ respectively, consistent with a highly fluorinated surface. Subsequent modification of the surface geometry using the aforementioned technique allowed us to rationally design surfaces with hierarchical scales of texture

that maximize the robustness of the composite interface (allowing lower surface tension liquids to be supported in the Cassie-Baxter state) and minimize the contact angle hysteresis (allowing liquid droplets to easily roll from the surface).

A complete list of measured contact angles on the different surfaces fabricated in this work is reported in Table 2.1. The nanostructures were deposited on both planar silicon and silicon microposts of varying dimensions, hereafter specified by the post diameter × the edge-to-edge spacing in micrometers. The deep reactive ion etching (DRIE) fabrication method for the microposts produced a characteristic scalloped profile on the vertical surfaces (Figure 2.2).[101] The nanotextures include planar ALD films, unbranched nanowires (NWs), and branched nanowires with decreasing "trunk" density, hereafter referred to as BNW-3, BNW-4, BNW-5, and BNW-7, with the number referring to the number of TiO_2 cycles in the overlayer (Table 2.1, Figure 2.8).

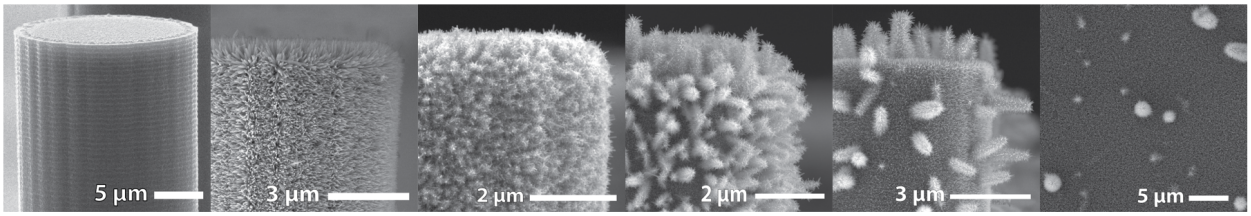

Figure 2.8: SEM images of representative samples from Table 2.1. From left to right: planar, unbranched NWs, BNW-3, BNW-4, BNW-5, and BNW-7.

To characterize the porosity of these disparate surfaces, we use the spacing ratio D^*.[40] D^* is effectively the inverse of the solid contact area ϕ_s, and in the case of these hierarchical arrays, it is given as:

$$D^* = \frac{4}{\pi}\left(\frac{(R+D)^2}{R^2}\right) \tag{2.1}$$

Here R and D refer to the size and spacing parameters shown in Figure 2.1. The apparent contact angle, θ^*, on a composite interface increases with increasing values of D^*. This is typically accompanied with a simultaneous reduction in the contact angle hysteresis. The Cassie-Baxter equation (Equation 1.6) can be re-written in terms of the spacing ratio as:

$$\cos\theta^* = -1 + \frac{1}{D^*}(1 + r_\phi \cos\theta) \tag{2.2}$$

For each level of additional texture, the D^* parameter can be determined by multiplying the D^* values of each individual scale of texture. For example D^* values for NWs on a micropost array would be $D^*_{microposts} \times D^*_{NWs}$ (Figure 2.1).

Planar ALD coated silicon microposts with low values of D^* (< 20), exhibit larger contact angle hysteresis even with the liquids that they are able to support in the Cassie-Baxter state. Their large planar tops are wetted by the liquids, resulting in a high values of ϕ_s, and subsequently larger contact angle hysteresis (for example, $\Delta\theta > 28°$ even for water). These samples are highlighted in Figure 2.9a,b within region i. Adding non-wetted, hierarchical texture significantly reduces the

Table 2.1: Contact angles on fluorosilanized samples with different combinations of microscale geometries (planar and microposts with varying spacing) and nanoscale geometries (planar ALD coatings, unbranched nanowires, and branched nanowires with increasing inter-nanowire spacing)

Nanoscale Geometry	Microscale geometry: Radius × edge-to-edge spacing (μm)	Contact angles (θ_a^*/θ_r^*,°)			
		Water	Hexadecane	Octane	Heptane
planar	planar	117/92	67/54	51/41	43/39
	post, 13×32	167/139	163/127	109/0	–
	post, 13×17	167/130	162/120	123/0	–
	post, 23×27	161/116	163/116	116/0	116/0
	post, 23×17	162/109	162/106	122/0	102/0
unbranched NWs	planar	172/166	108/0	–	–
	post 13×32	169/166	164/131	117/0	–
	post 13×17	167/163	165/116	158/101	–
	post 23×27	169/154	165/115	130/0	120/0
	post 23×17	170/161	162/99	162/99	113/0
BNW-3	planar	174/168	150/0	–	–
	post, 13×32	170/168	162/128	167/121	–
	post, 13×17	169/167	163/114	163/101	–
	post, 23×27	168/158	160/121	159/103	–
	post, 23×17	170/168	160/99	160/89	94/0
BNW-4	planar	173/169	161/102	144/0	–
	post, 5×45	172/170	166/156	162/145	160/130
	post, 5×30	172/170	164/152	162/142	159/130
	post, 13×32	171/169	165/146	162/119	161/110
BNW-5	planar	172/170	164/108	122/0	–
	post, 13×32	171/169	167/149	159/105	0/0
	post, 13×17	170/167	167/139	159/102	129/0
	post, 23×27	169/162	167/137	157/95	129/0
	post, 23×17	169/165	166/127	158/90	129/0
BNW-7	planar	174/171	135/0	–	–

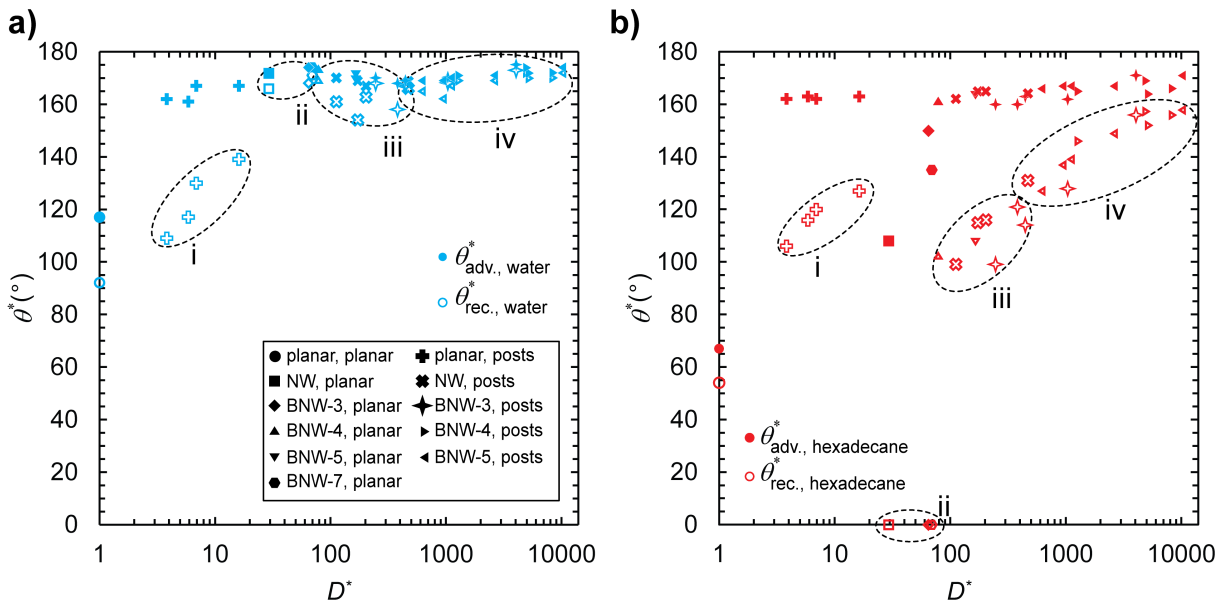

Figure 2.9: Advancing and receding contact angles with (*a*) water and (*b*) hexadecane versus the spacing ratio (D^*) for planar, unbranched, and branched NWs of varying density on planar and micropost substrates. Generally, contact angles increase and contact angle hysteresis decreases with increasing values of D^* as long as a composite interface is maintained. Samples may be separated into four groups based on their receding hexadecane contact angles as highlighted in the figure. (*i*) contains microposts without nanowires, exhibiting a high hysteresis Cassie-Baxter state with water and hexadecane. (*ii*) contains nanowires on planar substrates with insufficient re-entrant texture or which are too sparse, exhibiting the Wenzel state with hexadecane. (*iii*) contains hierarchical structures with lower receding hexadecane contact angles than the non-hierarchical posts in (*i*), due to nanotexture with insufficient re-entrance being wetted by hexadecane and (*iv*) contains hierarchical structures (mostly branched nanowires on microposts) with reduced hysteresis with hexadecane compared to (*i*).

contact angle hysteresis due to the decreased ϕ_s. The optimal samples are those with three levels of hierarchy, including BNW-4s and BNW-5s on microposts, located in region iv of Figure 2.9a,b. They produce significantly lower contact angle hysteresis with both water and hexadecane than planar ALD on posts ($\Delta\theta$ as low as ~1° and 10° respectively). As a consequence, low surface tension liquids readily roll or even bounce from these surfaces.

For a hierarchical texture to improve contact angle hysteresis over the microposts alone, the nano-texture itself must exhibit a greater receding contact angle with the liquid than a planar surface. For these highly rough nanotextures, this is equivalent to whether or not they maintain a composite interface with the contacting liquid. Liquids in the Wenzel state on nanowires exhibit effectively zero θ^*_r (*e.g.*, arrays of NWs or BNW-3s on planar substrates in Figure 2.9a,b, region ii). Hierarchical arrays of NWs or BNW-3s on microposts, therefore, exhibit hexadecane contact angle hysteresis values greater than those of planar microposts despite their significantly higher D^* (samples in Figure 2.9a,b region iii). However, as NWs and BNW-3s exhibit a robust composite interface with water, these samples exhibit very low hysteresis superhydrophobicity compared to planar coated

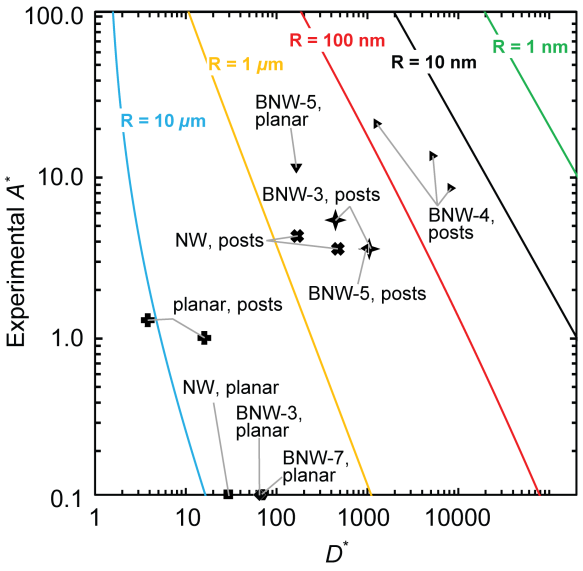

Figure 2.10: Robustness factor A^* measured with hexadecane droplet impact tests versus the spacing ratio D^*. The solid colored lines are theoretical A^* values for hexadecane calculated over varying inter-hoodoo spacing (D) for arrays of hoodoos, each corresponding to a fixed hoodoo cap radius, R, (labeled on the plot). For samples with the same type of texture, *e.g.*, planar ALD coated posts of varying inter-post spacing D, increasing D^* decreases the robustness of the composite interface, following this theoretical trend. To obtain excellent superomniphobicity, it is critical to circumvent this trade-off and simultaneously maximize A^* and D^*. This is done by introducing hierarchical texture – *e.g.*, unbranched nanowires on posts have increased A^* and D^* compared to planar ALD coated posts, and the A^*, D^* values for BNW-4s on posts, with three levels of hierarchy, are increased even further.

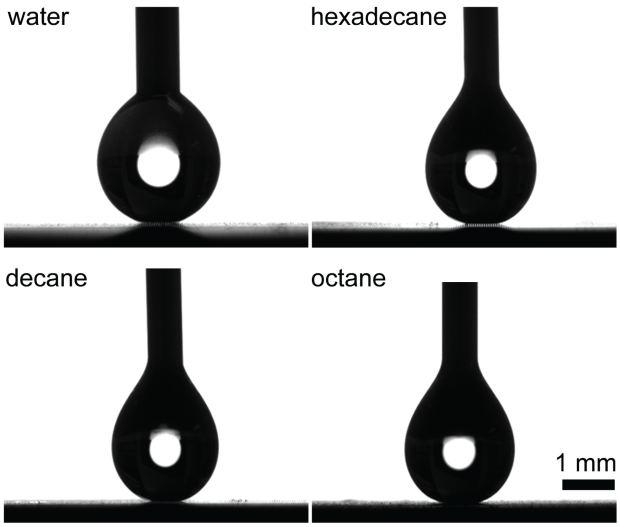

Figure 2.11: Representative photographs from the contact angle goniometer of the advancing contact angles with water, hexadecane, decane, and octane on a sample of BNW-4s on 13×32 posts.

microposts. To achieve low hysteresis superomniphobicity, therefore, it is not sufficient to add nanowires of any arbitrary geometry to a microstructured substrate.

As mentioned in the introduction, the robustness parameter, $A^* = P_b/P_{ref}$, may be used to characterize the resistance to wetting of superomniphobic surfaces.[5,6,77] Robust Cassie-Baxter states are characterized by $A^* \gg 1$. A^* may be directly measured or calculated for regular geometries. For the purposes of calculating robustness, the geometries produced in this work may be approximated as "micro-hoodoos", which are posts with overhanging horizontal caps.[6] As derived in our previous work, the robustness factor A^* for micro-hoodoos may be calculated as

$$A^* \approx \left(\frac{1}{H^*} + \frac{1}{T^*}\right)^{-1} \tag{2.3}$$

where

$$H^* = \frac{2R_{edge}\ell_{cap}\cos\theta}{D^2(1+\sqrt{D^*})}\left((1-\cos\theta) + \frac{H}{R_{edge}}\right) \tag{2.4}$$

and

$$T^* = \frac{\ell_{cap}\sin(\theta - \psi_{\min})}{D(1+\sqrt{D^*})} \tag{2.5}$$

where R_{edge} is the radius of curvature of the edge of the overhanging surface, D is the edge-to-edge spacing between post tops, R is the radius of the hoodoo caps, D^* is the spacing ratio defined in Equation 3, and ψ_{min} is the minimum texture angle for a given surface, which is defined from the horizontal such that it is 90° for a vertical wall, and 0° for the bottom of an overhang on a "micro-hoodoo".

A robust composite interface with very high breakthrough pressure is predicted by high values of the robustness factor ($A^* \gg 1$), while $A^* < 1$ indicates complete wetting. We have previously shown that the A^* parameter is capable of providing an *a priori* estimation of the stability of the composite Cassie-Baxter state on various textured surfaces.[5,40] In this work, A^* was determined experimentally by observing the lowest surface tension liquid supported in the Cassie-Baxter state, as well as by measuring breakthrough pressures with impacting hexadecane droplets (details in Methods section). If the inherent Young's contact angle (θ) for the contacting liquid on the planar surface falls below the ψ_{min}, the Cassie-Baxter state is no longer possible, as the net surface traction points downward into the texture. For example, the unbranched NWs on a planar substrate have a ψ_{min} close to 90°, and therefore only maintain water in the Cassie-Baxter state. On the etched posts (ψ_{min} ~55° due to the scalloped texture on the walls), water and hexadecane are supported in the Cassie-Baxter state, while lower surface tension liquids such as octane (γ_{LV} = 21.6 mN/m) are in the wetted state (*e.g.*, octane θ_a^*/θ_r^* = 109°/0° on 13×32 posts). Therefore, $A^* \gg 1$ for water and

hexadecane, while $A^* < 1$ for lower surface tension liquids such as octane. To allow these liquids to be maintained in the Cassie-Baxter state, the ψ_{min} values for the texture must be reduced.

The addition of a single level of NWs to the micropost arrays leads to an effective reduction in the average ψ_{min}, as the nanowire tips point horizontally from the post walls. This leads to an increased robustness of the Cassie-Baxter state with lower surface tension liquids, though the contact angle hysteresis for some low surface tension liquids increased relative to the unmodified posts due to wetting of the vertically oriented nanowires on the post tops, as previously discussed. On relatively closely spaced post arrays (lower D^*) with NWs, octane was observed to be in the Cassie-Baxter state (θ_a^*/θ_r^* = 158°/101° on 13×17 posts with NWs), but continued to wet sparser arrays (θ_a^*/θ_r^* = 117°/0° on 13×32 posts with NWs).

Generally, a higher fraction of downward facing NWs enables the average ψ_{min} to be closer to 0°, the value for a micro-fabricated hoodoo structure (on which all liquids with a finite contact should exhibit the Cassie-Baxter state). To demonstrate control over these geometric parameters, we demonstrate that branched NWs with sufficient spacing grown on microposts (Figure 2.7) yielded an increase in robustness over unbranched NWs on microposts. All post arrays coated in branched NWs yielded the Cassie-Baxter state with octane, and some even with heptane, whereas unbranched nanowires on posts with higher spacing were readily wet by octane. On samples with the optimum "trunk" spacing, (labeled as D_2 in Figure 2.1), even heptane could be supported in the Cassie-Baxter state with low enough hysteresis that it was mobile on the surface (γ_{LV} = 20.1 mN/m, θ_a^*/θ_r^* = 160°/130° on 5×45 posts with BNW-4s). However branched nanowires with denser or sparser "trunk" spacing (BNW-3 or BNW-5 respectively) yielded reduced robustness, and heptane was found to wet in all cases, again highlighting the need for tunable control of the hierarchical geometry at each length scale.

The results of the hexadecane droplet impact tests correlate with the decreasing surface tension of the liquids supportable in the Cassie-Baxter state (Figure 2.10). The robustness factor values generally increased from $A^* < 1$ for NWs and BNW-3s on planar substrates, to $A^* \approx 1$ for planar coated posts, to $A^* > 1$ for the various geometries that were wet only with heptane (unbranched NWs, BNW-3s, and BNW-5s on microposts). The A^* values increased further still for samples with the optimal three levels of hierarchy, *i.e.*, with BNW-4 on microposts. Figures 2.11 & 2.12a show the capability of this optimal surface to support a range of different low surface tension liquids in a robust Cassie-Baxter state. Figure 2.12b shows a hexadecane droplet bouncing completely from this surface, highlighting the low contact angle hysteresis (high D^* values) and high robustness to liquid breakthrough (high A^* values) obtained simultaneously on this optimal surface. The colored lines overlaid on Figure 2.10 are the theoretical A^* predictions for hexadecane calculated for arrays of hoodoos (ψ_{min} = 0°) with different fixed cap radii R, varying values of inter-hoodoo spacing D to yield varying spacing ratio D^* values, H = 30 μm, and R_{edge} = 25 nm. Note that for surfaces with a

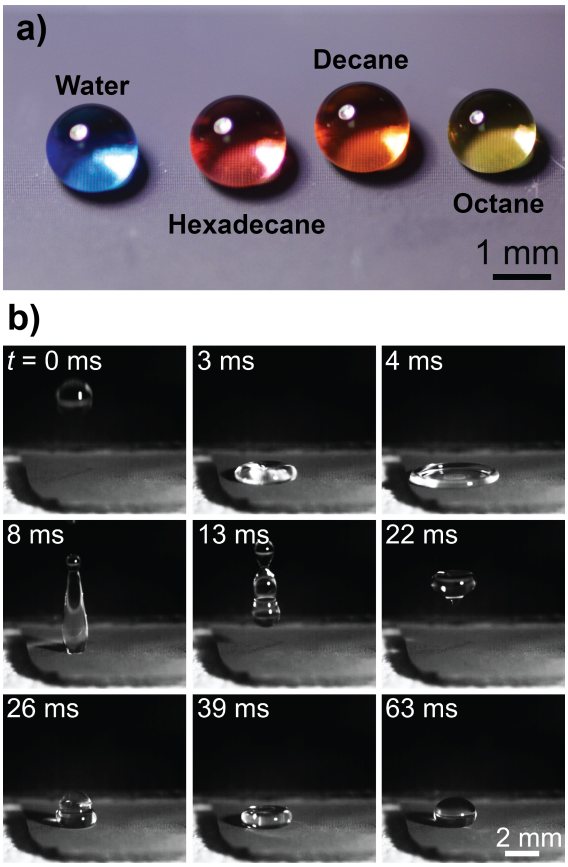

Figure 2.12: (*a*) Top: photograph of ~3 μL dyed liquid droplets on a micropost array with branched NWs (BNW-4s on 13×32). (*b*) Frames from a high-speed video of a ~10 μL hexadecane droplet completely bouncing from the sample in (*a*) after being dropped onto it from 5 cm.

single scale of texture, such as the micro-hoodoo surface, A^* is inversely proportional to D^*. This is also reflected in the experimental data for samples with varying micropost geometry but the same nanostructure (*e.g.*, BNW-4s on varying micropost arrays with varying dimensions). Ultimately, Figure 2.10 highlights how careful design and controlled fabrication of hierarchical texture can allow one to overcome this inherent tradeoff between contact angle and robustness on surfaces with a single scale of texture, and thereby simultaneously maximize both A^* and D^*.

2.5 Conclusion

Here we demonstrated a new method to programmably control individual geometric parameters in multi-level hierarchically branched nanostructures, using ALD to seed NW growth and modify material interfaces. This synthesis enables rational design and control of tunable superomniphobic surfaces, where the geometric parameters associated with feature size, separation, and orientation can be individually controlled for each level of hierarchy. While single-level NW arrays on planar substrates were sufficient to hold water in a Cassie-Baxter state and allow it to bounce off, additional levels of hierarchy were needed to design a surface that could also repel low surface tension liquids

such as hexadecane, octane, and heptane. The tunable control over contact angle and contact angle hysteresis demonstrates the power of this synthesis approach for the design and optimization of hierarchical nanostructures.

2.6 Acknowledgements

This material is based upon work supported by the National Science Foundation under the Graduate Research Fellowship Program under Grant No. DGE-1256260 as well as the Nanomanufacturing Program under grant #1351412. Support was also provided by Dr. Ki-Han Kim and the Office of Naval Research (ONR) under grant N00014-12-1-0874 and Dr. Charles Y. Lee and the Air Force Office of Scientific Research (AFOSR) under grant FA9550-15-1-0329. The S/TEM work was conducted in the William R. Wiley Environmental Molecular Sciences Laboratory (EMSL), a national scientific user facility sponsored by DOE's Office of Biological and Environmental Research and located at PNNL, which is operated by Battelle for the DOE under Contract DE-AC05-76RLO1830. Lithography was performed at the Lurie Nanofabrication Facility and SEM was performed at the Michigan Center for Materials Characterization (MC^2).

CHAPTER 3

Designing Self-Healing Superhydrophobic Surfaces with Exceptional Mechanical Durability

This chapter is primarily adapted from an article published in *ACS Applied Materials and Interfaces* which was equally co-authored with Kevin Golovin.[102]

3.1 Introduction

Superhydrophobic surfaces (SHSs) have garnered much attention over the last few decades for their ability to be self-cleaning,[1] drag-reducing,[2] stain-resisting,[3] and anti-fouling.[71] By trapping pockets of air in their porous texture, SHSs display water contact angles $\theta^* > 150°$ and low roll-off angles ($\theta_{roll\text{-}off}$).[6] The design and optimization of such surfaces have been well- studied.[1–3,5,6,40,62–69,71,103,104]

However, most natural and artificial SHSs suffer from poor mechanical durability, as their fragile and porous surface texture can be easily removed even by the swipe of a finger.[65] Only a few SHSs have been reported to exhibit mechanical durability, as characterized by sand impact,[57,105–108] rubbing with a soft cloth,[3,109–111] tape peel tests,[62,106,112–114] or sandpaper abrasion.[64,65,67–69,106,110,115–126] However, all such reports present single material systems. The development of design criteria to aid in the systematic fabrication of durable SHSs, generalizable to multiple chemistries or fillers, is expected to be extremely useful to the field. In the first part of this work, we develop such criteria.

Even the most durable SHSs will eventually become damaged by extreme or repeated mechanical abrasion, which damages a SHS's low surface energy and/or texture. SHSs that can regenerate both their surface texture and chemistry,[21,109,127] akin to the lotus leaf's ability to regenerate its nano-structured wax,[1] would be highly desirable. Herein we also report mechanically durable SHSs that exhibit physical and chemical self-healing. The developed surfaces can fully recover their water-repellency even after being abraded, scratched, burned, plasma cleaned, flattened, sonicated and chemically attacked. These surfaces, and the design parameters used to develop them, may find immediate usage in a wide range of academic and industrial sectors across the globe.

3.2 Fabrication Methods and Materials

3.2.1 Materials and Synthesis

All solvents, pre-polymers, and crosslinking agents were used as-received. Fluorinated solvents HCFC-225ca/cb (Asahiklin-225, Asahi Glass Co.) and HFC-43-10mee (Vertrel XF, DuPont) were purchased from Techspray and TMC Industries, respectively. Poly(methyl methacrylate) (PMMA), polystyrene (PS, 45 kDa or 1.2 kDa) and polyisobutylene (PIB) were purchased from Scientific Polymer. Luxecolor 4FVBA fluorinated polyol resin (FPU, 55% solids in n-butyl acetate) was purchased from Helicity Technologies. Desmophen 670BA polyol was provided by Covestro. Isocyanate crosslinkers Desmodur N3200 and Wannate HMDI (4,4'-Diisocyanato-methylenedicyclohexane) were provided by Covestro and Wanhua Chemical Group, respectively. Crosslinker ratios were 9.7 and 3.4 wt% respectively with FPU, and 28.5 wt% N3200 with 670BA. Propylene glycol, a chain-extending agent that increases the modulus of the final cross-linked polyurethane network, was obtained from MP Biomedicals. A polyurethane elastomer (Vytaflex 40) was purchased from Smooth-On, and was prepared according to manufacturer directions. CNR (chlorinated polyisoprene) was provided by Covestro. Poly(dimethyl siloxane) elastomer (Dow Corning Sylgard 184) was obtained from Krayden, and a 10:1 base:crosslinker ratio was used according to manufacturer directions. Acrylate-terminated perfluoropolyether resin (CN4001, purchased from Sartomer USA) was mixed with 5 wt% radical photoinitiator (Irgacure 2022, provided by BASF Corporation) to yield a UV-curable fluorinated polymer matrix. Cyanoacrylate adhesive (3M Scotch-Weld SF-100) was purchased from Pack-n-Tape. Two-part epoxy adhesive (Selleys Araldite 90 seconds) was used in an approximate 1:1 volume ratio of the components, per manufacturer instructions.

Fluorodecyl and fluorooctyl polyhedral oligomeric silsesquioxanes (F-POSS, FO-POSS) were prepared at the Air Force Research Laboratory by condensing perfluorinated triethoxysilanes, as previously reported.[128] Octaisobutyl polyhedral oligomeric silsesquioxane (IB-POSS) was purchased from Hybrid Plastics. Eicosane was purchased from Acros Organics.

3.2.2 Coating Sample Fabrication

Spray coating solutions were prepared by solubilizing the filler, polymer or pre-polymer, and cross-linker or photoinitiator (if applicable) at an overall solution concentration of 100 mg/mL. The fraction of filler in the total solution was varied from 0 to 50 wt%. The solvents used for F-POSS and FO-POSS blends were: pure Vertrel XF (for FPU and PFPE), pure AK-225 (for SF100, 670BA, PMMA, chain-extended FPU and PDMS), 50:50 Chloroform:Vertrel XF (for Vytaflex 40, PS and Araldite epoxy) and 50:50 AK-225:Hexane for PIB. Pure chloroform was used for IB-POSS blends with 670BA and FPU. Pure toluene was used for blends of eicosane and CNR.

No significant effect on spray coating morphology was observed between these solvents, as they have similar volatility and surface tension. The solutions were applied to 10 cm × 10 cm 6061 aluminum sheets with an ATD Tools 6903 high-volume-low-pressure spray gun. 20 mL of coating solution was applied to each plate, which resulted in coatings that were approximately 100 μm thick. However, because the surfaces were both porous and extremely rough, the thickness could not be well-defined, and during abrasion tests the percent mass loss was tracked instead (see below). Spray coated samples were held at room temperature for at least one day and then cured as necessary prior to further testing (polyurethanes: 80 °C for two days; PDMS: 150 °C for 1 h; epoxy and cyanoacrylate: room temperature for > 2 h; PFPE acrylate resin: 15 min simultaneous exposure to 254 and 365 nm UV mercury lamps under N_2 atmosphere).

3.3 Characterization Methods

3.3.1 Hansen Solubility Parameters

The miscibility of hydrophobic fillers within the polymeric binders was analyzed with the aid of the HSPiP software package and associated database of Hansen solubility parameters. All solvents were used without further purification, including acetone, THF, chloroform, ethylene glycol, toluene, cyclohexane, hexane, dodecane, DMSO, ethanol, n-butyl acetate, MEK and o-fluorotoluene (Fisher), as well as 1-hexanol, chlorobenzene, perfluorodecalin, hexafluorobenzene, p-chlorobenzotrifluoride, diisopropylamine, and pentafluorobutane (Sigma-Aldrich). Additionally, deionized water, AK-225, and Vertrel XF were used.

Cross-linked polymers and elastomers were swollen in a selected number of solvents until a consistent mass was achieved. Samples were weighed and then the solvent was extracted using a vacuum oven at 100 °C. The goodness of a solvent was determined by ranking the swelling ratio (divided by the mass of the solvent) from 1 to 6, with 1 assigned to solvents that swelled the polymer the most. These were then input into the HSPiP software in order to determine the center and radius of the given system, or to determine other solvents necessary to better define the radius of the Hansen sphere. The results of the Hansen sphere determination are tabulated in Table 3.1 (fillers), Table 3.2 (binders from this work), and Table 3.3 (binders from the HSPiP database).

3.3.1.1 The Hansen Miscibility Sphere for F-POSS

To determine the Hansen sphere for F-POSS, we found solubility maxima in a wide variety of fluorinated solvents. F-POSS is completely immiscible in all alkanes, whereas it dissolves in fluorinated alkanes to an extent, in agreement with the Hansen theory.[130] We evaluated seven pure fluorinated solvents (Table 3.1) and 27 mixtures of those solvents to get the F-POSS Hansen sphere (Figure 3.1a).

As stated in Section 3.2.2, we sprayed our coatings at a concentration of 100 mg/mL, and the

Table 3.1: Hansen Solubility parameters for the three previously unreported fillers determined in this chapter. Hansen parameters for IB-POSS (18.0 ± 0.1, 2.1 ± 0.2, 2.7 ± 0.3, 4.3) were sourced from the literature.[129]

	F-POSS	FO-POSS	Eicosane
Water	×	×	×
Ethanol	×	×	×
Ethylene Glycol	×	×	×
Hexanol	×	×	–
Acetone	×	×	×
Chlorobenzene	×	×	–
Chloroform	×	×	✓
THF	×	×	–
MEK	×	×	×
MIBK	×	×	✓
nBA	×	×	✓
Toluene	×	×	✓
Cyclohexane	×	×	✓
Hexane	×	×	✓
Dodecane	×	×	✓
Diisopropylamine	×	×	✓
Asahiklin-225	✓	✓	–
Vertrel XF	✓	✓	–
Perfluorodecalin	✓	×	–
DMF	×	×	×
DMSO	×	×	×
Acetic acid	×	×	–
Hexafluorobenzene	✓	✓	–
o-Fluorotoluene	×	×	–
p-Chlorobenzo-trifluoride	×	×	–
Pentafluorobutane	×	✓	–
PGMEA	-	-	×
δ_D (MPa$^{1/2}$)	14.7 ± 0.1	13.6 ± 0.1	15.9 ± 0.3
δ_P (MPa$^{1/2}$)	0.0 ± 0.8	1.9 ± 0.6	3.0 ± 0.6
δ_H (MPa$^{1/2}$)	0.0 ± 1.2	0.0 ± 0.5	3.9 ± 0.4
R_o (MPa$^{1/2}$)	3.2	5.1	6.0

Table 3.2: Hansen parameters for the five previously unreported binders evaluated in this work.

	FPU	FPU-PG	PFPE	SF-100	Vytaflex 40	Desmophen 670BA
Water	×	×	×	×	×	×
Ethanol	×	×	×	×	×	×
Ethylene Glycol	×	×	×	×	×	×
Hexanol	×	–	×	×	×	×
Acetone	✓	✓	×	✓	✓	✓
Chlorobenzene	✓	✓	×	✓	✓	✓
Chloroform	✓	✓	×	✓	✓	✓
THF	✓	✓	×	✓	✓	✓
MEK	✓	✓	×	✓	✓	✓
nBA	✓	✓	×	✓	✓	✓
Toluene	✓	✓	×	✓	✓	✓
Cyclohexane	×	×	×	×	×	×
Hexane	×	×	×	×	×	×
Dodecane	×	×	×	×	×	×
Diisopropylamine	×	×	×	✓	×	-
Asahiklin-225	✓	✓	✓	✓	×	✓
Vertrel XF	×	×	✓	×	×	×
Perfluorodecalin	×	×	✓	×	×	×
DMF	×	–	×	✓	×	✓
DMSO	×	–	×	✓	×	✓
Acetic acid	✓	–	–	-	✓	-
δ_D (MPa$^{1/2}$)	16.0 ± 0.2	17.3 ± 0.4	12.6 ± 0.2	17.1 ± 0.3	18.0 ± 0.5	18.0 ± 0.7
δ_P (MPa$^{1/2}$)	9.5 ± 0.5	7.0 ± 0.7	4.4 ± 0.8	7.2 ± 0.3	4.9 ± 0.6	8.7 ± 0.6
δ_H (MPa$^{1/2}$)	3.6 ± 0.5	4.6 ± 1.2	0.1 ± 1.2	6.4 ± 0.4	9.9 ± 1.0	5.9 ± 0.8
R_o (MPa$^{1/2}$)	9.3	5.2	5.1	8.4	4.4	8.4

Table 3.3: Hansen solubility parameters for binders present in the HSPiP database.

	PMMA	PS	PIB	PDMS	Araldite (Epoxy)	Pergut (CNR)
δ_D (MPa$^{1/2}$)	18.6	18.9	16.9	17	14	17.4
δ_P (MPa$^{1/2}$)	10.5	8.1	2.5	2.9	7.4	9.5
δ_H (MPa$^{1/2}$)	5.1	4.6	4.0	2.6	9.4	3.8
R_o (MPa$^{1/2}$)	8	10.3	7.2	5.7	13.7	10

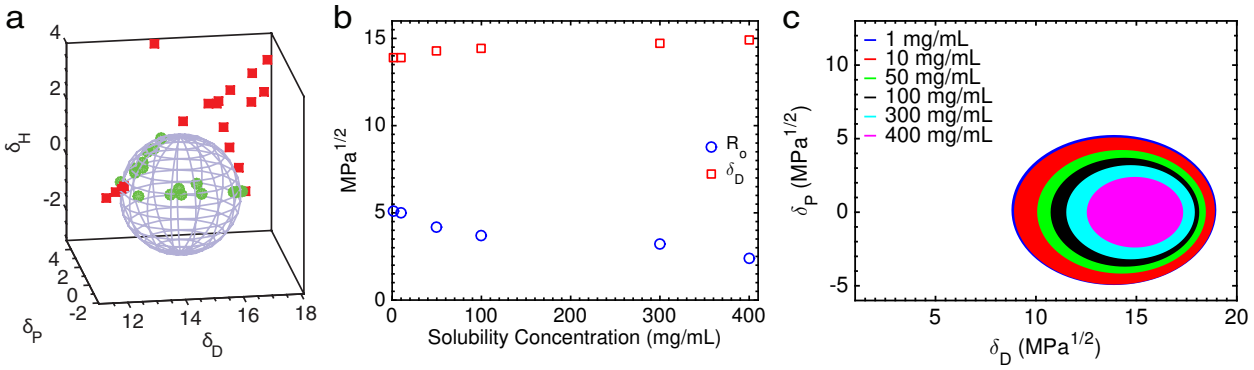

Figure 3.1: Solubility data for F-POSS. (*a*) The Hansen sphere for F-POSS, constructed using seven pure fluorinated solvents and 27 mixtures. See Table 3.1 for the coordinates of the sphere. (*b*) The Hansen radius and dispersive component as a function of F-POSS solubility concentration. As expected, forcing higher concentrations of F-POSS to be solubilized decreased the radius of the sphere, and shifted the center closer to the best solvent, hexafluorobenzene. (*c*) The change in F-POSS radius and dispersive component as a function of concentration. Other than the 1 mg/mL concentration, all other spheres had essentially no polar or H-bonding components. The 1 mg/mL sphere was centered at ($\delta_D = 13.88 \pm 0.05$, $\delta_P = 0.15 \pm 0.55$, $\delta_H = 0.60 \pm 1.10$ MPa$^{1/2}$). The radius was $R_o = 5.1$ MPa$^{1/2}$.

highest percentage of F-POSS in any coating was 50 wt%. Thus, our method for ranking F-POSS solubility was as follows: Any solvent that dissolved at least 50 mg/mL F-POSS was ranked a 1 (in the HSPiP program), and any solvent with less than 1 mg/mL solubility was ranked a 6. Solvents with F-POSS solubility in between these limits were graded from values of 2–5 based on interpolation. Because F-POSS has essentially no polar or H-bonding components, trends between concentration, radius and dispersive components became apparent (Figure 3.1b). We also modified our rankings for different concentrations, which effectively shrank the sphere and shifted it towards better solvents for F-POSS as the concentration was increased (Figure 3.1c).

The highly perfluorinated arms of the POSS cage make both the polar and hydrogen bonding solubility parameters of F-POSS effectively zero. However, for consistency, we always chose the Hansen sphere that maximized the fit and minimized the residuals, for both F-POSS and all binders evaluated. This is why we report values of 0.03 MPa$^{1/2}$ for both polar and hydrogen bonding components of F-POSS (Table 3.1). Careful mixtures of solvents with identical dispersive components, but slightly differing polar and hydrogen bonding components, confirmed that F-POSS is only dispersive in nature. Moreover, although the dispersive component of F-POSS was found to be $\delta_D = 14.26 \pm 0.1$ MPa$^{1/2}$, by far the best solvent for F-POSS is hexafluorobenzene. Hexafluorobenzene appears close to the edge of the F-POSS Hansen sphere due to the approximation of the hydrogen bonding parameter. In 3-parameter Hansen space, $\delta_H^2 = 2\delta_a\delta_b$, where δ_a is the proton acceptor component, and δ_b is the proton donor component.[131] Thus, although many fluorinated solvents are known to have large proton donor components,[132] most have a zero proton acceptor component, resulting in a net zero hydrogen bonding parameter.

3.3.2 Wettability Analysis

3.3.2.1 Dynamic Contact Angles

Advancing and receding contact angle measurements were obtained via the sessile drop method using a Ramé-Hart 200 F1 contact angle goniometer. A water droplet suspended from a vertical dispensing needle was brought into contact with the substrate, and its volume increased and decreased to obtain the advancing and receding contact angles. A circular drop profile on the live video feed in the DROPImage Advanced software was used to obtain contact angle data. At least three points were measured across the substrate for each reported contact angle. Droplet roll-off angles, $\theta_{roll\text{-}off}$, were obtained by placing at least five 25 μL water droplets distributed across the surface with a micropipette, and using the manual tilting stage of the goniometer to gradually increase the angle. The tilt angle was recorded when each droplet rolled off, and the average across the droplets was calculated. Droplets that did not roll off were recorded as $\theta_{roll\text{-}off} = 90^\circ$ for averaging purposes. Large error bars were observed for some abraded samples, which arose from averaging areas that wet with areas that remained superhydrophobic.

3.3.2.2 Breakthrough Pressure

Pressure stability was measured both statically and dynamically. Static pressure testing was done using a pressure tank (TCP Global) with a 7 cm head of deionized water. The pressure was regulated using compressed air. Samples were submerged and the pressure was raised to the set level for 60 seconds at a ramp rate of no more than 5 psi/s. After the pressure was released, samples were removed to determine if they remained dry. Due to the inhomogeneity of the surfaces, breakthrough was considered to have occurred when the sample was fully wetted upon removal from the water tank. Dynamic pressure testing was done using impacting water droplets and a high-speed camera (Fastec Imaging HiSpec 1) at 2,000 frames per second. Breakthrough was considered to have occurred when the droplet did not rebound from the surface upon impact. As the maximum droplet height for our experimental setup was 1.7 m, corresponding to an impact velocity of 5.7 m/s, many surfaces exhibited breakthrough pressures too high to measure using droplet impact.

3.3.3 Imaging and Metrology

Scanning electron micrographs were obtained with a Philips XL30 SEM after sputter coating the samples with gold to reduce charging effects. Two-dimensional height-maps (2.4 mm × 2.4 mm) of the surfaces were obtained with an Olympus LEXT OLS4000 3D Laser Measuring Microscope with a 10× objective, and at least five height maps were collected for each reported data set. This data was subsequently analyzed to yield statistical topographical parameters using MATLAB (see

Section 3.4.2 below). The root-mean-squared roughness, S_q, was found using

$$S_q = \sqrt{\frac{1}{xy}\sum_x \sum_y h_{x,y}^2} \tag{3.1}$$

where $h_{x,y}$ is the height of the surface at point (x,y), after the mean height has been set to zero.

3.4 Design Criteria

3.4.1 The Miscibility Parameter (S^*)

The lowest possible surface energy, $\gamma_{SV} \approx 9$ mN/m, is achieved with a monolayer of $-CF_3$ groups.[23] Chemically grafting such monolayers requires specific substrate chemistry. Moreover, the thin monolayer only renders the uppermost surface hydrophobic, and any surface degradation will expose the higher surface energy material underneath. In contrast, the incorporation of highly perfluorinated compounds within a coating allows one to achieve equally low surface energies without the need for chemical grafting.[128,130] Moreover, these unbound species can diffuse to the surface, restoring the low surface energy after mechanical or chemical attack, thereby reducing the formation of hydrophilic defects upon damage.[65] Such coatings can be universally applied to any substrate, and impart low surface energy throughout the entire thickness of the coating. In this work, we fabricated a library of SHSs using sprayed blends of polymeric binders and hydrophobic fillers. Due to its low surface energy, $\gamma_{SV} \approx 10$ mN/m, we primarily focused on systems incorporating 1H,1H,2H,2H-heptadecafluorodecyl polyhedral oligomeric silsesquioxane (F-POSS),[128] although the developed design parameters are generalizable to other material systems, as we show. Spray coating was chosen as the primary methodology for the application of the superhydrophobic coatings because it is inexpensive, scalable, and allows control over the surface energy and texture of our coatings via simple changes in experimental parameters.

The cohesive energy of any material species can be broken into its dispersive, polar, and hydrogen bonding Hansen solubility parameters, (δ_D, δ_P, δ_H).[130] A miscibility sphere can be experimentally constructed for any compound, with its center at some point in a 3D space defined by these three solubility parameters, and its volume encompassing all good solvents and excluding all poor solvents. We first determined the miscibility spheres for several hydrophobic fillers and a wide variety of binders (Figure 3.2), by screening their solubility in a large number of solvents (Tables 3.1-3.3).

The overlap between the Hansen spheres of the binder and filler is indicative of their chemical compatibility, and the extent to which they phase separate and form texture during the spray-coating process. In order to quantify a polymer's miscibility with the filler, we developed the miscibility parameter S^*, which is given as

$$S^* = \frac{\Delta R - R_{binder} + R_{filler}}{2R_{filler}} \tag{3.2}$$

Here, ΔR is the distance in 3D solubility space between the centers of the filler's sphere and the

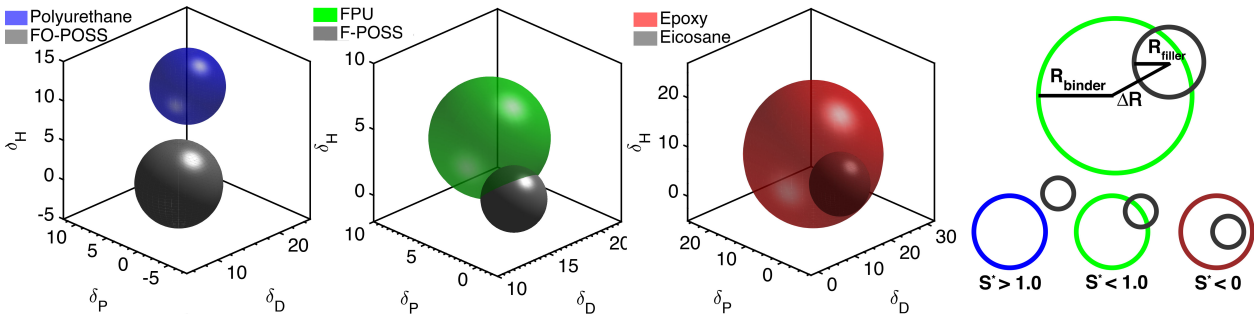

Figure 3.2: Visualization of the S^* parameter for three binders in 3D Hansen space. FO-POSS: fluorooctyl polyhedral oligomeric silsesquioxane. FPU: fluorinated polyurethane. F-POSS: fluorodecyl polyhedral oligomeric silsesquioxane.

binder's sphere, with their radii denoted by R_{filler} and R_{binder}, respectively.

Similar to Hansen's Relative Energy Difference value,[130] S^* is defined such that the filler is completely immiscible with a binder when the two spheres do not overlap ($S^* > 1.0$, also see schematic in Figure 3.2). Alternately, binders with $S^* < 0$ have solubility spheres that completely encompass the filler's sphere, and are hence fully miscible (at a given concentration, see Figure 3.1). In between these two extremes is the regime of partial miscibility. As we show below, this behavior greatly affects the ability of an SHS to maintain water repellency after mechanical abrasion (Section 3.5.1).

The S^* parameter allows one to predict whether the filler will phase separate from the binder during spray coating. This phase separation manifests in the sprayed surface's root-mean-squared roughness, S_q. For example, we determined the solubility spheres for a polyurethane and an epoxy, which are both commonly used hydrophilic adhesives (Tables 3.2 and 3.3). For the epoxy, $S^* \approx 0.2$ with F-POSS, and an epoxy + 5 wt% F-POSS blend, when sprayed, resulted in a smooth surface with $S_q = 0.8$ μm. Conversely, for the polyurethane, $S^* \approx 1.6$, and a polyurethane + 5 wt% F-POSS blend, when sprayed in the exact same manner, resulted in a very rough surface ($S_q = 41$ μm). The polymer matrices used in this work were always smooth when sprayed by themselves as described above. Thus, immiscibility alone can induce roughness during the spray coating process. However, a large S_q does not guarantee superhydrophobicity.[133]

3.4.2 The Superhydrophobic Potential (P^*)

Water on SHSs can exist in the Cassie-Baxter state, in which air pockets are trapped in the surface's porous texture.[35] However, water can displace these air pockets, leaving the surface in a wetted, Wenzel state.[33] SHSs should ideally be designed such that the Cassie-Baxter state is energetically preferred.[1] We developed a method to predict when the Cassie-Baxter state would be energetically favorable over the Wenzel state using only the topographical statistics of a given surface. Because each binder/filler combination exhibited a distinct, characteristic surface morphology, we wished to

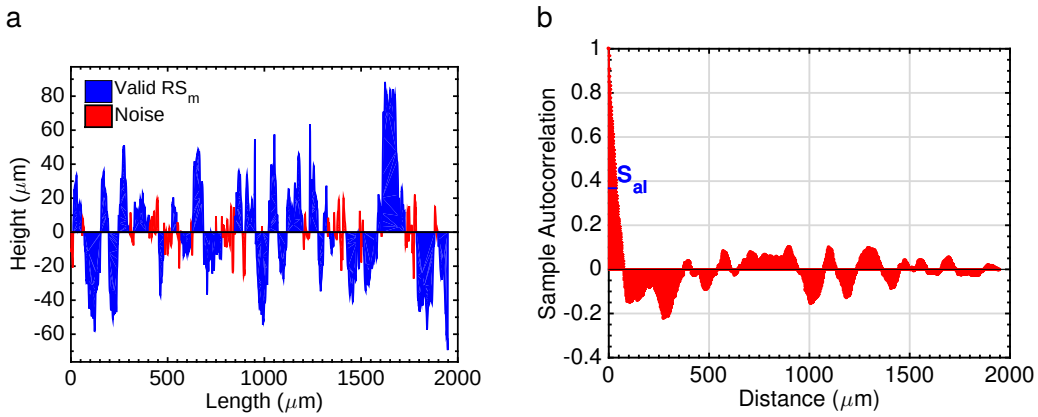

Figure 3.3: (*a*) The parameter RS_m is shown by filling in each periodic 'element'. (*b*) The autocorrelation function of a surface versus the distance along the surface examined. In this work, a value of e^{-1} was used as a cutoff.

develop universal metrics that characterize surfaces with widely varying topographies. To do so, we measured three statistical surface properties: peak periodicity, RS_m, auto-correlation length, S_{al}, and the Wenzel roughness, r.[33]

RS_m represents the length along the surface between large surface features, and can be thought of as the center-to-center distance between texture elements.[134] RS_m is defined as,

$$RS_m = \frac{1}{m}\sum_{i=1}^{m} X_i \tag{3.3}$$

where X_i is the length of a peak (Figure 3.3a).[135] A peak was defined such that its height is $> 10\%$ of the maximum height, and its length is $> 1\%$ of the total sampling length. This allows one to separate genuine texture features from noise. In Figure 3.3a the noise and valid X_i are labeled.

The second statistical parameter, S_{al}, is the shortest autocorrelation length. An autocorrelation function can be constructed for any surface by evaluating the self-similarity of heights when small perturbations in distance are made.[133] In effect, S_{al} represents the distance at which a peak becomes a valley or vice versa. In this work we used the popular cutoff in the autocorrelation function of e^{-1} (Figure 3.3b). Before defining the porosity of random surfaces using the above statistical parameters, we first briefly make the connection to the canonical surface of micro-pillars. Such surfaces are often studied for their simple geometry but relatively good water repellency. Square pillars can be defined by their width $2R$ and the spacing in between pillars $2D$ (Figure 3.4). If water is placed on such a surface (with $\theta \geq 90°$), it may be able to support a composite solid-liquid-air interface, which will be contingent upon the dimensions of R and D. Should the composite interface be stable, the fraction of solid in contact with the air is given by $\phi_s = 2R/(2R + 2D)$ in the one dimensional case. Converting to two dimensions simply involves squaring ϕ_s.

For a randomly rough surface we must resort back to the statistical lengths of RS_m and S_{al}. The one-dimensional solid fraction may be defined as $\phi_s = S_{al}/RS_m$. In our previous work,[5] we found it

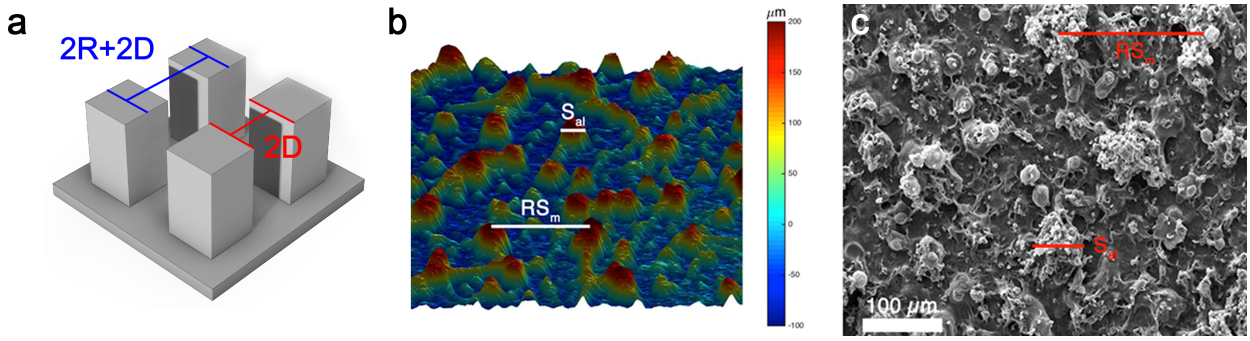

Figure 3.4: (*a*) A diagram illustrating the dimensions R and D on a simple pillar array surface. Representations of RS_m and S_{al} on (*b*), a LEXT height-map, and (*c*), an SEM of a randomly textured spray-coated surface.

instructional to define the porosity of a surface as the inverse of ϕ_s,

$$D^*_{stat} = (RS_m/S_{al})^2 \tag{3.4}$$

where the second power is added to convert from properties measured along one-dimensional height profiles to the porosity of a two-dimensional surface.[6] Larger values of D^*_{stat} indicate surfaces with higher porosity. Note that we use the two dimensional form, and that we average the measured RS_m and S_{al} values over the entire two-dimensional surface.

For the Cassie-Baxter state to be favored over the wetted, Wenzel state, it must be the global energy minimum.[136] For a given surface topography, the free energies of the two states can be balanced (*i.e.*, equating Equation 1.3 with Equation 1.6). The non-wetted state is energetically preferred only if the intrinsic contact angle, θ_E, exceeds a critical value, θ_c. This critical intrinsic contact angle is given by[136]

$$\cos\theta_c = (\phi_s - 1)/(r - \phi_s) \tag{3.5}$$

where ϕ_s is the fraction of solid in contact with water (note $D^*_{stat} \approx \phi_s^{-1}$, and we assume $r_\phi = 1.0$). Stated differently, and recalling that intrinsic water contact angles cannot exceed 120°,[5] there exists some minimal texture that any surface, regardless of chemistry, must exhibit in order to achieve an energetically favorable Cassie-Baxter state. Substituting this maximum contact angle as θ_c yields,

$$\cos\theta_c = \cos 120^\circ = (1/D^*_{stat} - 1)/(r - 1/D^*_{stat}) \tag{3.6}$$

or

$$-0.5 = (1 - D^*_{stat})/(rD^*_{stat} - 1). \tag{3.7}$$

We can then define a surface's superhydrophobic potential, P^*, such that only for values of $P^* < 1.0$ is the Cassie-Baxter state the global energy minimum. Doing so yields,

$$P^* = 2(D^*_{stat} - 1)(rD^*_{stat} - 1). \tag{3.8}$$

For any surface that exhibits $P^* > 1.0$, the wetted state is energetically preferred, regardless of surface chemistry. Note that water can exist in a metastable Cassie-Baxter state through the addition of re-entrant texture,[5] and hence a value of $P^* > 1.0$ does not necessarily indicate wetting. P^* is useful because surfaces are often created with a given topography, and then subsequently rendered superhydrophobic by applying a low surface energy layer on top.[1] As such, measuring P^* allows one to determine *a priori* if such a surface will become superhydrophobic before applying such a (often expensive) low surface energy monolayer. Moreover, if a surface is superhydrophobic in spite of a $P^* > 1.0$ value, one can say with certainty that water will exist in a metastable state, and such a surface should be used with caution. By measuring the dynamic contact angles on many surfaces, both wetted and non-wetted, we probed the effectiveness of P^*.

When water initially advances on a SHS, it displays θ_a^*.[137] If any texture elements become wetted, the apparent angle at which water recedes, θ_r^*, will be much lower than θ_a^*. Thus, θ_a^* can be thought of as a measure of the SHS's inherent porosity (*i.e.*, fraction of air pockets), ignoring how stable the air pockets may be, and θ_r^* gives an indication of their stability.[54] We measured θ_r^* for more than fifty combinations of F-POSS and various polymeric binders, as a function of P^* (Figure 3.5a). These binders included both cross-linked networks, such as urethanes, acrylates, epoxies, and cyanoacrylates, as well as linear polymers such as polystyrene, polymethylmethacrylate and polyisobutylene (Section 3.2, Table 3.4). We observed a high θ_r^* only for systems with a stable Cassie-Baxter state, *i.e.*, $P^* < 1.0$. This was confirmed by the sharp jump in θ_r^* at a value of $P^* = 1.0$. The specific value of $P^* = 1.0$, corresponding to an intrinsic contact angle $\theta_E \approx 120°$, indicated that all the surfaces had a high percentage of F-POSS at the solid-liquid interface, although there were vast differences in topography. Thus, we were able to predict if an F-POSS-containing surface could be superhydrophobic solely by measuring P^*. Without measuring P^*, there is no easy way to determine if a randomly textured surface has the potential to become superhydrophobic, *a priori*.

Moreover, for surfaces with $P^* < 1.0$, recasting the Cassie-Baxter relation (Equation 1.6)[35] in terms of D_{stat}^* effectively predicted θ_a^* (Figure 3.5b). We observed that the predictive power of D_{stat}^* and P^* extended to other SHSs not containing F-POSS. These SHSs included polymer blends with other hydrophobic fillers like eicosane, octa-isobutyl POSS (IB-POSS) and fluoro-octyl POSS (FO-POSS), as well as other SHSs such as three commercially available superhydrophobic formulations (Section 3.2, Tables 3.1-3.3), lithographically fabricated microstructures,[60] textured metals treated with self-assembled monolayers,[138,139] and binders filled with hydrophobic particles.[140] As such, the design parameters developed in this work are applicable to SHSs produced using a wide range of binders, fillers, and fabrication techniques.

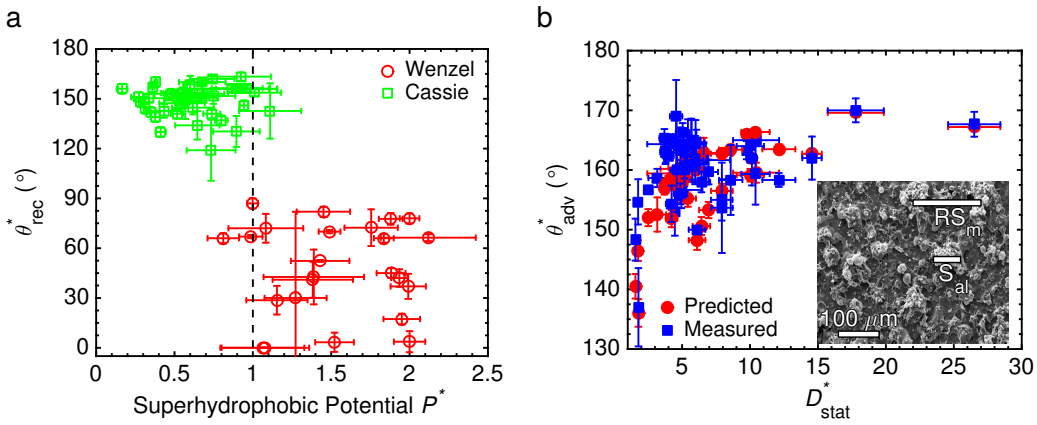

Figure 3.5: (*a*) The apparent receding contact angle versus the P^* parameter. The sharp transition at $P^* = 1.0$ is consistent with an intrinsic contact angle of $\theta_E = 120°$. (*b*) Measured and predicted apparent advancing contact angles versus the statistical porosity parameter, D^*_{stat}. This plot includes all the different systems from Table 3.4. The inset shows an SEM micrograph of the FPU + 15 wt% F-POSS sprayed surface, with representative RS_m and S_{al} values indicated.

3.5 Durability of Superhydrophobic Surfaces

3.5.1 Overview of Abrasion Testing

We utilized the industry standard of rotary Taber abrasion (Section 3.5.2) to evaluate the mechanical durability of our sprayed binder/filler blends. The stresses generated by Taber abrasion can be estimated using a cylinder-cylinder Hertzian contact mechanics analysis (Figure 3.6a, Section 3.5.3).[141] Depending on the elastic modulus of the coating, the exerted shear stress ranged from tens to hundreds of kilopascals (Figure 3.6a). Due to the porosity of the surface, the texture elements experienced shear stresses on the order of a few megapascals. This is similar or greater than the less systematic durability characterization techniques employed in the literature.[64,65,67–69,106,110,115–126] For example, in a recent report,[69] a durable SHS was abraded with sandpaper along a total length of 800 cm, without degradation of high contact angle. We reproduced such an evaluation for our FPU/F-POSS blend, which maintained high contact angles, as well as low roll-off angles, even after 1 kilometer (100,000 cm) of abrasion using the same sandpaper and applied load (Figure 3.7). Thus, we are confident that the surfaces created in this work can also withstand other metrics of mechanical durability reported elsewhere. The details of these two testing methods are included below.

One hundred rotary Taber abrasion cycles was sufficient to differentiate durable and non-durable SHSs, *i.e.*, non-durable surfaces were either completely removed or wetted by water after 100 abrasion cycles. For each binder with a given S^* we varied P^* by adjusting the amount of hydrophobic filler in the blend. Combining the S^* and P^* parameters allowed us to construct a phase diagram for the different possible surfaces created when spraying the binder/filler blends (Figure 3.8). Here we

denote surfaces with a (×) when the water roll-off angle was $\theta_{roll\text{-}off} > 15°$ (not superhydrophobic), and surfaces that exhibited $\theta_{roll\text{-}off} < 15°$ (superhydrophobic) as (■) if not durable or (●) if durable. These two regions were demarcated by a line at $P^* = 1.0$, *i.e.*, we never observed a SHS for which $P^* > 1.0$.

Only surfaces that exhibited $\theta_{roll\text{-}off} < 15°$ after 100 abrasion cycles are shown as green circles (●) in Figure 3.8. All such surfaces exhibited partial miscibility with the hydrophobic fillers ($0 \leq S^* \leq 1.0$). Low surface energy species are known to preferentially migrate to the solid-air interface.[4] For binders with $S^* > 1.0$, the final surface was always very mechanically weak, with a powdery consistency, because the filler was completely immiscible with such binders. Finally, we noted that increasing the amount of filler within a sprayed blend was not always efficacious. As the binder can be much more mechanically resilient than the filler molecules, any excess filler within the blend, beyond what is required to achieve superhydrophobicity ($P^* < 1.0$), can lower the overall durability. For example, a perfluorinated polyether, PFPE, with 25 wt% F-POSS remained superhydrophobic after abrasion, but PFPE with 35 wt% F-POSS did not, although the S^* and P^* values were equivalent. Overall, choosing components that satisfy $S^* < 1.0$ helps ensure that the final surface will be durable, and choosing a sufficient filler content such that $P^* < 1.0$ assures that the surface will exhibit a robust Cassie-Baxter state. We then continued Taber abrasion of our partially miscible blends (Table 3.4).

3.5.2 Abrasion Testing Methods

Abrasion testing, based on ASTM standard D4060, was performed with a Taber Model 5135 Rotary Abraser with CS-10 resilient abrasive wheels. 250 g weights were placed on the rear of the wheel arms such that the applied normal load was 60 g. The sample was then rotated relative to the freely spinning abrasion wheels such that a shearing abrasion action occurred within a defined area. Excess debris was removed continuously with a vacuum nozzle just above the substrate. The result was a

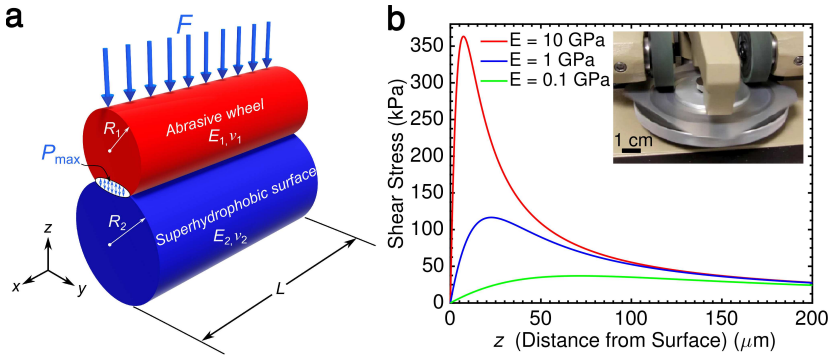

Figure 3.6: A schematic of the forces experienced during Taber abrasion, estimated using Hertzian contact mechanics, assuming a cylinder/cylinder configuration (see Section 3.5.3.[141] (*b*) The shear stress experienced during Taber abrasion as a function of depth into the coating. The inset shows the rotary Taber abraser.

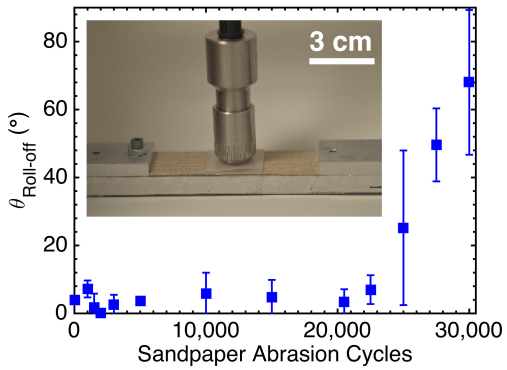

Figure 3.7: The 25 μL water roll-off angle for the FPU/F-POSS coating versus the number of sandpaper abrasion cycles, mimicking a previously reported durability characterization.[69] The inset shows the linear Taber abrasion machine, modified to perform sandpaper abrasion.

ring-shaped region on the sample that was consistently mechanically damaged.

The manual sandpaper abrasion test which is commonly performed in the literature, such as in [69], was automated using a Taber Model 5750 Linear Abraser. A 2.5 × 2.5 cm spray coated sample was mounted facing downwards on the reciprocating head, and brought in contact with 240 grit sandpaper, with an applied load of 250 g. The sample was then moved laterally under load across the sandpaper, and the test was continued until water droplets were pinned. Water roll-off angles were measured periodically to confirm the retention of superhydrophobicity (Figure 3.7b).

3.5.3 Derivation of Hertzian Contact Mechanics of Rotary Taber Abrasion

Although it is an industrial standard for measuring the mechanical durability of coatings, Taber abrasion has rarely been used to evaluate superhydrophobic surfaces. Here we briefly show the relevant contact stresses involved in Taber abrasion. During the abrasion process, two wheels are constantly rubbed against the coated surface. According to Hertzian contact mechanics, this situation can be modeled by cylinder/cylinder contact (Figure 3.6a), in which the lower surface is given an infinite radius of curvature.[141] In such a case, the area of contact between the abrading wheel and the coated surface is an ellipse, with half-width b given as,

$$b = \sqrt{\frac{4RF[E_2(1-\upsilon_1^2) + E_1(1-\upsilon_2^2)]}{\pi L E_1 E_2}} \tag{3.9}$$

Here R is the radius of the wheel (49 mm), F is the normal load (60 g), L is the length of abrasion (10 mm), and E_1, υ_1, E_2, and υ_2 are the elastic moduli and Poisson ratios of the wheel and coating, respectively. The maximum pressure exerted on the coating is given as,

$$P_{max} = 2F/\pi bL \tag{3.10}$$

Although this pressure can compress the surface, the main degradation occurs because of the shear stresses generated. If we define x as the direction tangential to the rotation during Taber

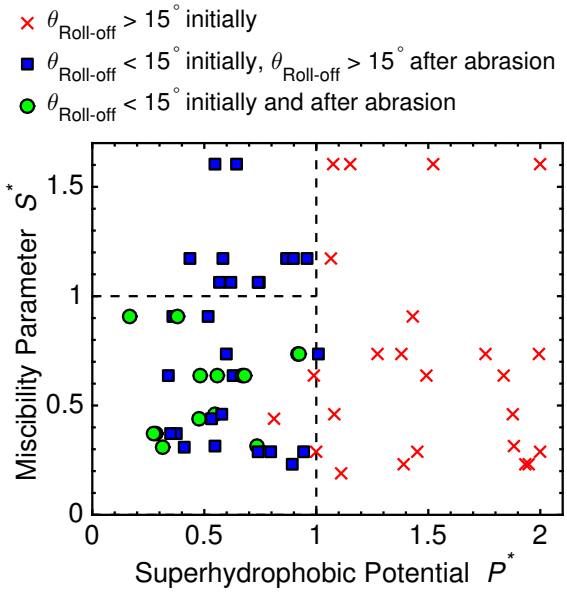

Figure 3.8: A design parameter phase diagram for all the surfaces developed in this work (see Table 3.4). Only surfaces with $P^* < 1.0$ can be superhydrophobic ($\theta_{roll\text{-}off} < 15$ °), and additionally only surfaces with $S^* < 1.0$ can be mechanically durable ($\theta_{roll\text{-}off} < 15$ °after 100 abrasion cycles). The non-SHS that exhibited $P^* < 1.0$ was a blend of FPU/FO-POSS. For this blend, $\theta_E = 91°$, although the sprayed texture required $\theta_c = 114°$. This is an example of sufficient texture for an SHS but insufficiently low surface energy.

abrasion, and z as normal to the coating, the principal stresses are given as,

$$\sigma_x = -2\upsilon_2 P_{max}\left[\sqrt{\frac{z^2}{b^2}+1} - |z/b|\right] \tag{3.11}$$

and

$$\sigma_z = -P_{max}(z^2/b^2+1)^{-1/2} \tag{3.12}$$

and finally, the shear stress in the xz-direction (the direction of abrasion) is

$$\tau_{xz} = \frac{1}{2}|\sigma_x - \sigma_z| \tag{3.13}$$

These stresses are dependent on the modulus of the coating, measurable using standard tensile testing.[142] Using the modulus measured for FPU resulted in a maximum shear stress experienced of $\tau_{xz} \approx 120$ kPa. Solving for the solid fraction via the Cassie-Baxter equation using the contact angles of water on our surfaces gives a local shear stress of a few MPa at the texture elements during abrasion.

3.5.4 Abrasion Testing Results

We compared the durability of these systems to three commercially available, and purportedly durable, SHSs (Figure 3.9a). None of the commercial coatings maintained a low $\theta_{roll\text{-}off}$ after 100 abrasion cycles. We extended the abrasion testing of our partially miscible binder/filler blends exhibiting $0 < S^* < 1$ and found them to be quite resilient to mechanical wear (Figure 3.9b). Whereas

all other evaluated SHSs became wettable within 100 abrasion cycles, the non-wetting properties of our surfaces fabricated from partially miscible, spray-coated blends endured significantly longer.

When blended with F-POSS, coatings incorporating the PFPE, SF-100, and FPU binders remained superhydrophobic for up to about 400, 500, and 800 Taber abrasion cycles, respectively. Combinations of the polyurethane Desmophen 670BA and IB-POSS, or the FPU and FO-POSS, both exhibited $\theta_{roll\text{-}off} < 15^\circ$ for $\approx$ 800 cycles. In fact, all such systems only became wettable once almost the entire coating was abraded away. For example, a 100 μm-thick FPU/F-POSS coating maintained $\theta_{roll\text{-}off} < 15^\circ$ even when > 90 μm of its thickness was removed. Note that the coating mass loss was not linear with the number of abrasion cycles, as larger loosely-adhered aggregates were removed first.

Table 3.4: Surface properties of the coatings developed in this work, before and after 100 rotary Taber abrasion cycles.

	F-POSS			Initial	Initial	Initial	100 cycle	100 cycle	100 cycle	100 cycle
Base	(%)	P^*	D^*_{stat}	θ^*_a (°)	θ^*_r (°)	$\theta_{roll\text{-}off}$ (°)	θ^*_a (°)	θ^*_r (°)	$\theta_{roll\text{-}off}$ (°)	mass loss (%)
NeverWet	-	1.79	7.4	165	162	1	132	32	54	17
Ultra Ever Dry	-	1.36	4.	161	152	1	155	0	90	14
Cytonix WX 2100	-	1.04	1.4	164	156	18	122	77	90	6
FPU (S^* = 0.64)	0	1.84	7.2	115	66	55	-	-	-	-
FPU	1	0.99	14.3	106	67	90	106	63	90	1
FPU	3	1.49	25.5	121	66	90	122	78	76	3
FPU	5	0.31	1.5	148	112	62	151	102	75	8
FPU	10	0.34	2.5	162	150	10	159	124	22	20
FPU	15	0.48	3.9	165	159	2	161	154	2	32
FPU	20	0.56	3.5	163	153	5	161	144	10	40
FPU	25	0.67	6.4	166	153	2	164	152	2	86
FPU	30	0.68	4.8	165	160	2	163	144	3	81
FPU	35	0.63	4.4	160	151	1	146	113	24	56
FPU-PG (S^* = 1.06)	5	0.62	5.3	163	145	8	153	98	81	44
FPU-PG	10	0.57	8.2	161	152	7	158	116	57	40
FPU-PG	15	0.75	4.7	162	148	7	161	113	90	27
FPU-PG	20	0.74	5.6	164	151	3	159	123	40	26
PMMA (S^* = 1.17)	0	1.06	5.1	155	0	90	-	-	-	-
PMMA	2	0.76	5.5	160	83	14	135	0	90	109
PMMA	5	0.43	4.0	160	143	11	149	123	35	99
PMMA	10	0.58	3.4	163	153	7	159	128	24	104
PMMA	35	0.90	5.9	166	156	2	162	127	26	129
PMMA	50	0.86	4.2	164	156	0	127	84	63	100
SF-100 (S^* = 0.74)	0	1.99	2.9	93	37	64	-	-	-	-
SF-100	5	1.38	3	129	41	90	-	-	-	-
SF-100	10	1.75	2.9	140	72	83	-	-	-	-
SF-100	15	1.27	4.5	158	123	13	167	113	37	22
SF-100	20	1.01	3.8	163	157	1	165	164	1	55
SF-100	25	0.92	3.5	169	163	0	166	164	1	55
SF-100	35	0.60	7.0	167	159	2	145	107	34	38

PDMS (S^* = 0.32)	0	1.88	3.8	123	45	90	-	-	-	-
PDMS	15	0.73	5.4	154	119	47	158	137	10	20
PDMS	30	0.55	5.4	160	153	4	157	0	66	46
PFPE (S^* = 0.46)	0	1.88	18.6	113	78	53	-	-	-	-
PFPE	5	2.12	0.5	127	66	66	-	-	-	-
PFPE	15	1.08	7.0	155	72	47	163	20	90	45
PFPE	25	0.55	3.7	156	147	7	163	142	8	33
PFPE	35	0.58	4.1	165	153	2	164	0	90	100
Vytaflex (S^* = 1.60)	0	2.00	1.0	74	4	90	-	-	-	-
Vytaflex	1	1.52	9.6	149	0	90	-	-	-	-
Vytaflex	5	1.08	4.5	150	0	90	-	-	-	-
Vytaflex	10	1.15	3.1	135	29	90	-	-	-	-
Vytaflex	15	0.65	4.5	158	134	11	159	55	39	28
Vytaflex	35	0.55	5.2	160	150	2	161	130	17	-
PS 45 (S^* = 48)	0	1.15	29.6	157	123	14	-	-	-	-
PS 45	15	0.60	1.9	157	131	14	156	114	37	26
PS 45	25	0.58	1.4	155	142	15	152	111	38	14
PS 1.2 (S^* = 0.48)	15	0.94	8.5	159	153	0	-	-	-	-
PIB (S^*0.19)	0	1.27	19.3	118	61	90	-	-	-	-
PIB	15	1.18	10.4	164	143	14	161	118	90	48
Araldite (S^* = 0.23)	0	1.95	2.9	101	17	90	-	-	-	-
Araldite	5	1.94	12.5	128	43	90	127	62	87	-
Araldite	15	1.39	1.0	137	43	90	132	69	90	3
Araldite	25	0.89	9.0	158	130	14	158	16	90	25
Desmophen (S^* = 0.91)	0	1.43	41.9	85	49	90	-	-	-	-
Desmophen	2.5	0.52	8.9	161	141	8	148	94	74	17
Desmophen	5	0.36	7.8	166	157	5	159	125	23	20
Desmophen	10	0.38	8.4	166	160	4	162	129	16	24
Desmophen	15	0.17	2.3	165	156	9	164	162	2	27

	FO-POSS			Initial	Initial	Initial	100 cycle	100 cycle	100 cycle	100 cycle
Base	(%)	P^*	D^*_{stat}	θ^*_a (°)	θ^*_r (°)	$\theta_{roll\text{-}off}$ (°)	θ^*_a (°)	θ^*_r (°)	$\theta_{roll\text{-}off}$ (°)	mass loss (%)
FPU (S^* = 0.44)	15	0.81	8.9	141	66	90	137	68	90	4
FPU	25	0.53	7.2	163	149	9	161	124	30	12
FPU	35	0.48	7.0	162	153	4	162	146	14	15

	IB-POSS			Initial	Initial	Initial	100 cycle	100 cycle	100 cycle	100 cycle
Base	(%)	P^*	D^*_{stat}	θ^*_a (°)	θ^*_r (°)	$\theta_{roll\text{-}off}$ (°)	θ^*_a (°)	θ^*_r (°)	$\theta_{roll\text{-}off}$ (°)	mass loss (%)
FPU (S^* = 0.31)	25	0.41	5.1	165	130	15	140	75	90	9
FPU	30	0.31	4.9	164	144	5	165	132	15	17
Desmophen (S^* = 0.37)	2.5	0.52	5.7	139	57	90	129	46	90	5
Desmophen	5	0.36	8.6	158	96	81	137	46	90	8
Desmophen	10	0.35	6.6	164	142	13	160	66	90	20
Desmophen	15	0.38	7.8	163	139	14	150	91	61	16
Desmophen	25	0.28	5.8	165	148	8	165	136	15	21
Desmophen	30	0.27	5.8	166	151	10	165	155	6	24

	Eicosane			Initial	Initial	Initial	100 cycle	100 cycle	100 cycle	100 cycle
Base	(%)	P^*	D^*_{stat}	θ^*_a (°)	θ^*_r (°)	$\theta_{roll\text{-}off}$ (°)	θ^*_a (°)	θ^*_r (°)	$\theta_{roll\text{-}off}$ (°)	mass loss (%)
CNR (S^* = 0.29)	0	2.00	18.3	93	78	90	-	-	-	-
CNR	25	1.45	11.3	157	82	84	-	-	-	-

CNR	30	1.00	3.5	162	87	71	-	-	-	-
CNR	35	0.74	4.3	153	161	14	162	92	33	2
CNR	40	0.80	3.4	148	137	15	163	113	38	3
CNR	50	0.94	6.5	160	146	11	164	77	90	11

As further proof that partial miscibility is required for mechanically durable SHSs, we chain-extended the FPU by incorporating propylene glycol into the cross-linked network (Section 3.2). The chain-extended FPU exhibited a three-fold increase in elastic modulus. A smooth film of chain-extended FPU exhibited a 12% reduction in mass loss during abrasion as compared to unmodified smooth FPU. However, the increased number of urethane linkages altered the Hansen sphere for the cross-linked network, changing the miscibility with F-POSS from $S^* \approx 0.6$ to $S^* \approx 1.1$. As such, whereas a sprayed blend of FPU + 15 wt% F-POSS ($P^* = 0.48$) remained superhydrophobic after 800 abrasion cycles, a sprayed blend of the chain-extended FPU + 15 wt% F-POSS ($P^* = 0.56$) was no longer superhydrophobic after only 100 abrasion cycles (Figure 3.9b). This counterintuitive result emphasizes the fact that the binder with the correct miscibility $0 \leq S^* \leq 1.0$, even if not necessarily the most mechanically durable binder, is more likely to yield a mechanically durable SHSs. Moreover, the blend of FPU/F-POSS also withstood a host of other potentially damaging exposures. After ultrasonication, a fluoro-solvent rinse, acid and base immersion, knife scratching, accelerated weathering, ultraviolet exposure, and heating at 350 °C for 3 days, the coating always maintained $\theta_{roll\text{-}off} < 15°$.

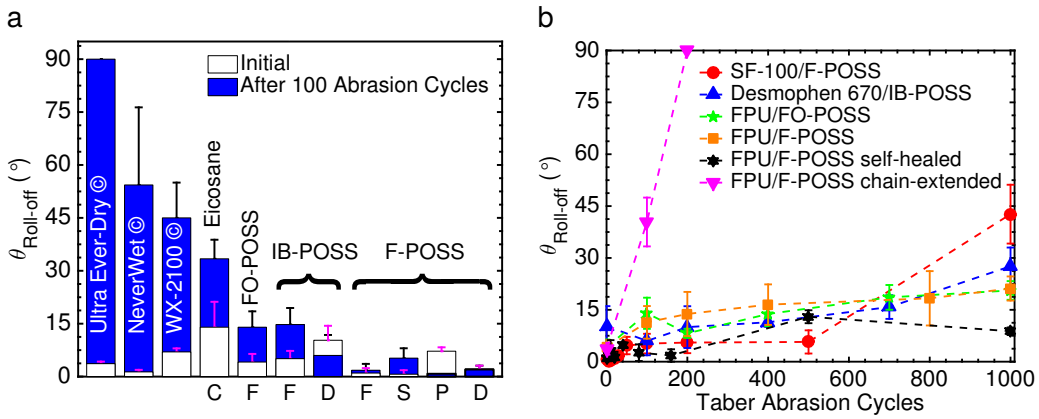

Figure 3.9: (*a*) The roll-off angles for three commercially available SHSs and eight of the SHSs fabricated in this work ($S^* < 1.0$), initially and after 100 abrasion cycles. C: chlorinated rubber, F: FPU, D: Desmophen 670BA, S: SF-100, P: PFPE. (*b*) The droplet roll-off angles for four representative durable SHSs fabricated in this work. The data for the propylene glycol chain-extended FPU/F-POSS and the self-healed FPU/F-POSS are also shown.

3.5.5 Abrasion Does Not Induce Superhydrophobicity

As Taber abrasion was employed to remove surface features, we wished to verify that the abrasion process was not itself inducing roughness and aiding the retention of superhydrophobicity. To do

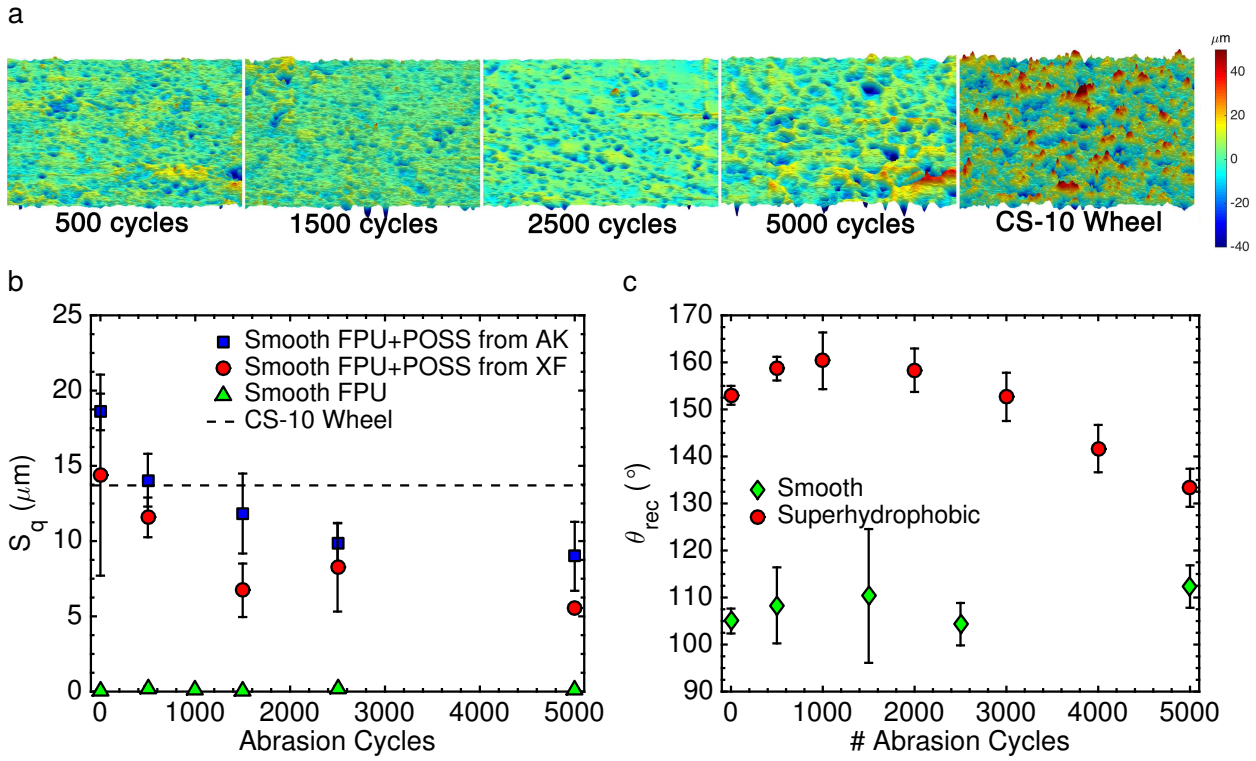

Figure 3.10: (*a*) Heightmaps of a smooth FPU + 15 wt% F-POSS film spin-cast in Vertrel XF, versus the number of Taber abrasion cycles. (*b*) Root-mean-squared height of smooth FPU + 15 wt% F-POSS, spin-cast from either Asahiklin-225 (AK) or Vertrel XF (XF). Smooth FPU without F-POSS, sprayed from $CHCl_3$, is shown for comparison, along with the CS-10 wheel. (*c*) The receding contact angle of the FPU + 15 wt% F-POSS in XF coating, either smooth or rough, as a function of abrasion. (*a-c*) support that the abrasion process did not induce superhydrophobicity.

so, we spin-cast relatively smooth films of FPU + 15% F-POSS using two solvents. Due to solvent evaporation effects, the surfaces retained some texture (Figure 3.10a,b). For another comparison, we sprayed a smooth film of pure FPU.

We measured the roughness of the abrasive CS-10 wheel. If the abrasion process were imprinting the texture of the wheel into the coating, the roughness of the coating would eventually reach the roughness of the wheel. We tracked the roughness (Figure 3.10b) of the smooth FPU and FPU + 15% F-POSS films over 5,000 abrasion cycles. Contact angles were also measured for the FPU + 15% F-POSS film spin-cast in XF (Figure 3.10c). The spin-cast FPU + 15% F-POSS films became smoother than the wheel with increasing abrasion and the receding contact angle did not significantly increase. Moreover, the pure FPU, which initially displayed $S_q = 155 \pm 70$ nm, only increased to $S_q = 650 \pm 100$ nm after 1,000 abrasion cycles. These results confirm that the abrasion process does not induce texture necessary for superhydrophobicity.

3.6 Other Durability Characterizations and Self-Healing

3.6.1 Overview

The low surface energy of fillers such as F-POSS causes them to migrate to the solid/air interface,[4] imparting some of the binder/filler blends with a robust, self-healing nature, enabling survival of extended abrasion testing. The details of these tests are described in the following sections. We focused on one of the most durable coatings, the FPU binder blended with 15 wt% F-POSS and subjected it to a broad range of damaging exposures. In most cases, there was only negligible increase in $\theta_{roll\text{-}off}$ observed (Figure 3.11). In cases where damage was observed, the fabricated coating can both chemically and physically self-heal, due to the surface migration of F-POSS upon heating, and the elastomeric nature of the FPU ($T_g \ll$ room temperature).

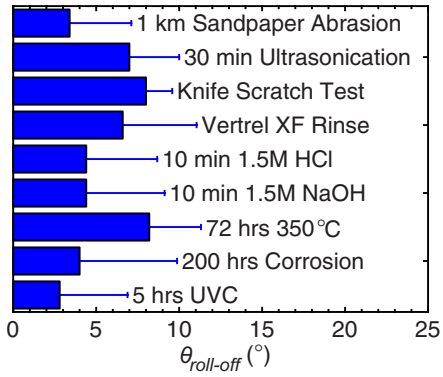

Figure 3.11: Additional durability characterizations that the FPU + 15 wt% F-POSS coating could withstand without self-healing.

3.6.2 Extended Abrasion with Healing

The FPU + 15 wt% F-POSS coating maintained $\theta_{roll\text{-}off} < 15°$ up to about 800 abrasion cycles (Figure 3.9). Beyond this, $\theta_{roll\text{-}off}$ increased with the number of abrasion cycles. But if the coating was placed on a 100 °C hotplate for a few minutes, the water repellency was easily restored ($\theta_{roll\text{-}off} < 5°$, Figure 3.12). With self-healing, the FPU/F-POSS coating maintained $\theta_{roll\text{-}off} < 15°$ even after 4,000 abrasion cycles. This was expected after measuring the statistical properties of the surface after self-healing, which always yielded $P^* < 1.0$ (Figure 3.13). Other blends created using different elastomers, such as SF-100/F-POSS, FPU/FO-POSS, or Desmophen 670BA/IB-POSS, also exhibited a self-healing nature. The self-healing and superhydrophobic nature of Desmophen 670BA/IB-POSS system is notable because neither of the components contains any fluorinated species.

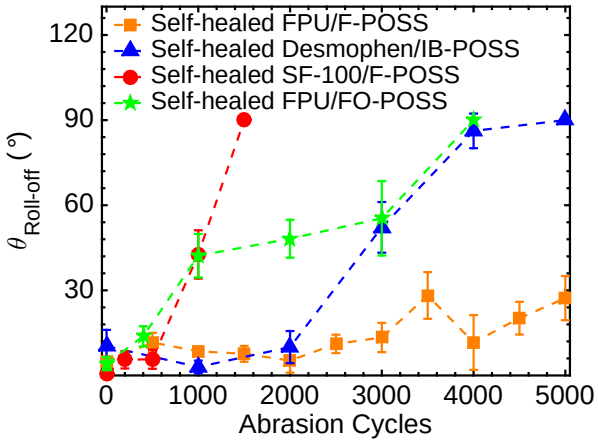

Figure 3.12: The roll-off angle for four binder/filler blends after self-healing, as a function of the number of abrasion cycles.

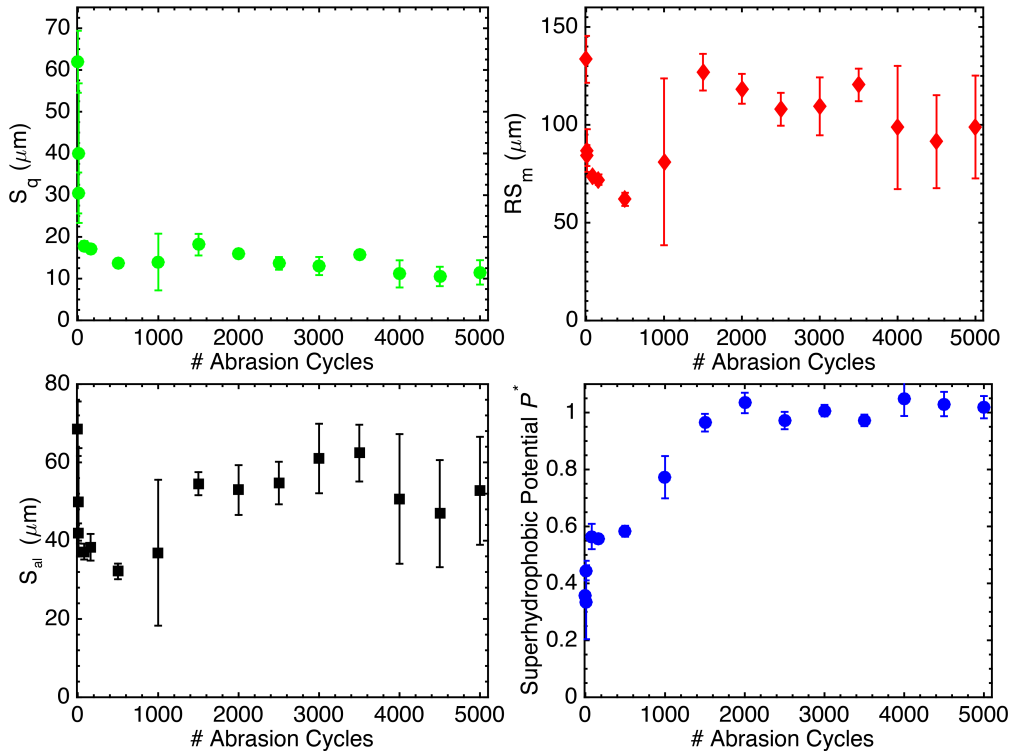

Figure 3.13: The four statistical parameters characterizing the FPU + 15 wt% F-POSS spray-coated blend, as a function of the number of Taber abrasion cycles.

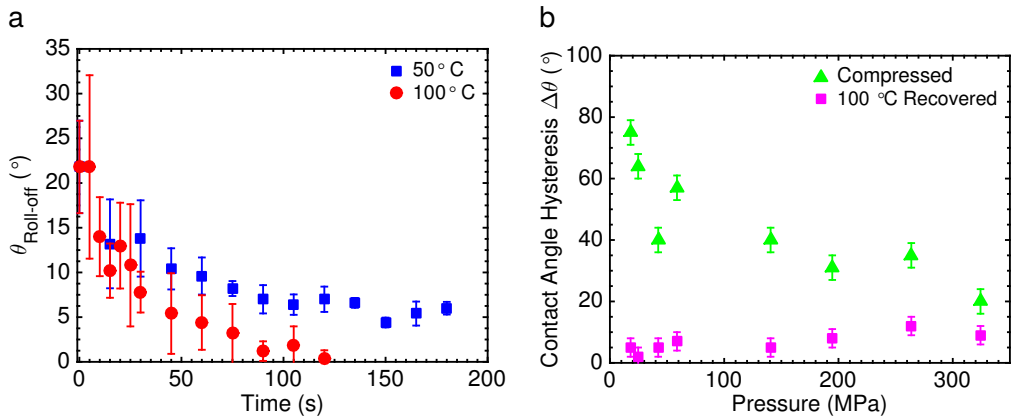

Figure 3.14: Texture recovery. (*a*) The self-healing properties of the FPU/F-POSS coating as a function of time and temperature, after 1,000 Taber abrasion cycles. S_q increased from 2.6 μm to 3.3 μm during self-healing. (*b*) The contact angle hysteresis for the FPU/F-POSS coating before and after thermal recovery from compression, as a function of the compressive load. Note that the coating $\Delta\theta$ decreased with an increase in applied load because the surface became smoother after compression. All compressed surfaces were fully wetted.

3.6.3 Physical Self-Healing after Abrasion or Compression

The thermal recovery of low surface energy due to F-POSS migration will only result in a SHS if the texture is also maintained. Although abrasion damages the texture of the FPU/F-POSS coating, we found that the abraded texture was still sufficient for superhydrophobicity (Figure 3.12). Further, we also observed that the texture could be partially restored during the thermal treatment. For example, after 1,000 abrasion cycles, the FPU/F-POSS coating exhibited S_q = 2.6 μm. Thermal recovery at 100 °C for 120 seconds increased this value to S_q = 3.3 μm (measured at identical locations) (Figure 3.14a). Thus, abrasion also slightly compressed the coating.

To further explore this, we subjected the coating to compressive stresses up to 350 MPa using a Carver 4350 compression molder with a 30 ton capacity. Samples of known dimensions were placed between aluminum plates and a variable pressure up to 350 MPa was applied and held for 60 seconds. The contact angles were then measured immediately following compression. Following compression, the sample was heated on a 100 °C hotplate for 5 minutes, and contact angles were recorded again. Although flattening the texture elements significantly reduced the texture of the coating and eliminated its superhydrophobicity ($P^* \approx 2.0$, Figure 3.14b), such damage was reversible, and upon heating, the coating quickly recovered its original porous texture ($P^* \approx 0.6$, Figure 3.14b, 3.15). Environmental scanning electron microscopy (ESEM) allowed us to observe this self-healing *in situ* (Figure 3.15b). As the compression set (percentage of permanent strain after compression) of elastomers is typically non-zero, the use of elastomeric materials in the fabrication of SHSs may be advantageous in terms of their ability to recover from compressive stresses that remove their porous texture.

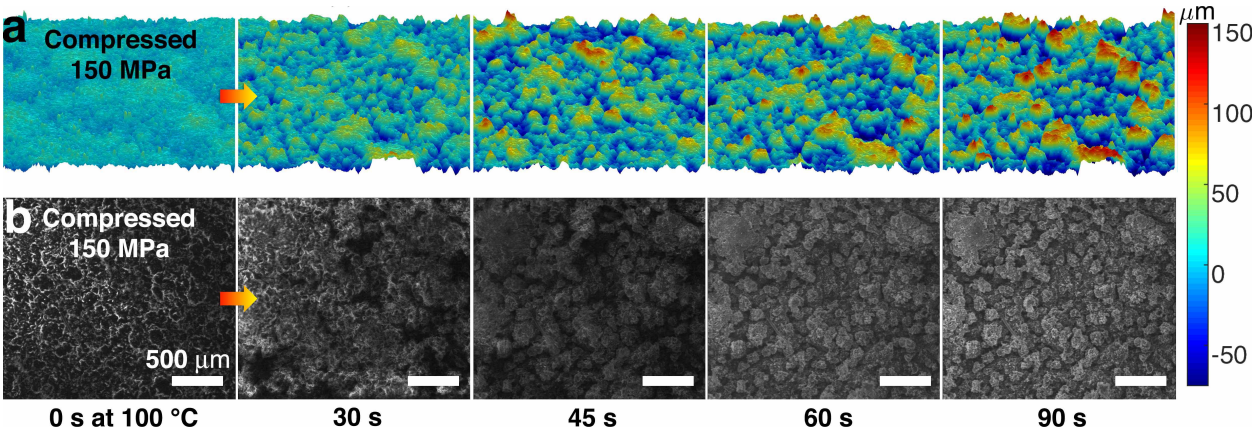

Figure 3.15: (*a*) Height maps of the FPU/F-POSS coating after 150 MPa compression, as a function of recovery time at 100 °C. (*b*) The recovery of the texture was also imaged *in situ* using environmental scanning electron microscopy.

3.6.4 Thermal Degradation Analysis

A sample of FPU + 15 wt% F-POSS was placed on a hot plate at temperatures from 150–425 °C, increasing by 25 °C for every hour of the test. After each annealing step, the dynamic contact angles were measured (Figure 3.16a). To correlate the onset of degradation of the Cassie-Baxter state with chemical degradation of the sample, thermogravimetric analysis was performed with a TA Instruments Discovery Series TGA using ~6 mg samples scraped from the same spray-coated surface. These samples were either held at a fixed temperature of 150 °C – 450 °C for 1 h (inset, Figure 3.16a), or heated from 25–600 °C at 10 °C/min in a 10 mL/min N_2 gas purge flow while continually monitoring its mass. The coating maintained low $\theta_{roll\text{-}off}$ when held at temperatures up to about 350 °C, the point at which the FPU+F-POSS material begins to degrade (Figure 3.16b). However, even at temperatures where > 75% of the mass would degrade, the coating maintained $\theta_{roll\text{-}off} < 15°$. (Figure 3.16b).

3.6.5 UV and Oxygen Plasma Exposure

To demonstrate resistance to irradiation damage, a sample of FPU + 15 wt% F-POSS was placed under 254 nm UVC at a distance of 5 cm. The contact angles were measured after five hours of continuous exposure, showing minimal change (Figure 3.11). A more aggressive test utilized oxygen plasma, which hydrolyzes F-POSS,.[143] A sample of FPU + 15 wt% F-POSS was exposed to O_2 plasma (Harrick Plasma PDC-001) using an RF source power of 30 Watts and a pressure of ~ 200 mTorr for 20 min. This rendered the FPU/F-POSS coating completely hydrophilic ($\theta^* = 0°$), although P^* remained unchanged as the low power plasma did not affect the coating texture. To recover the water repellency, the coated surface was heated on an 80 °C hotplate, and the $\theta_{roll\text{-}off}$ periodically measured. Upon heating, the low surface energy and superhydrophobicity was fully restored (Figure 3.17a). The time required for full superhydrophobic recovery decreased with

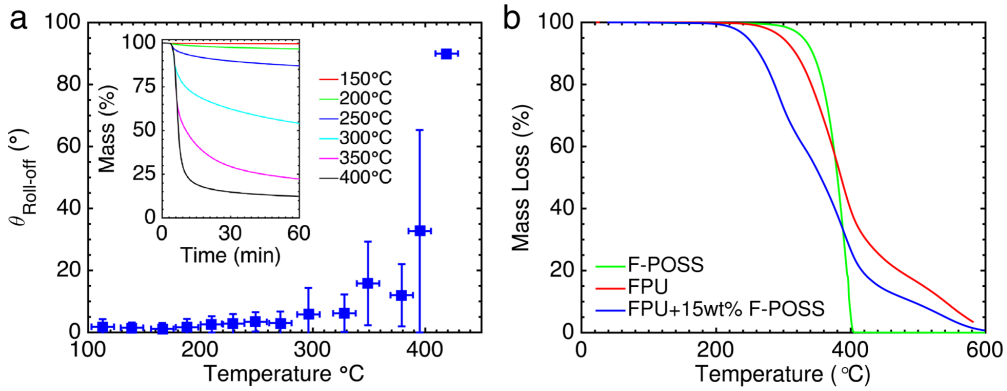

Figure 3.16: (*a*) The roll-off angle of a sample of the FPU + 15 wt% F-POSS coating versus cumulative 1 h annealing steps. The inset shows isothermal TGA of the same coating, at different temperature points, showing severe mass loss only occuring above 250 °C. (*b*) TGA (10 °C/min) ramp for pure F-POSS, pure FPU and the blend of FPU + 15 wt% F-POSS.

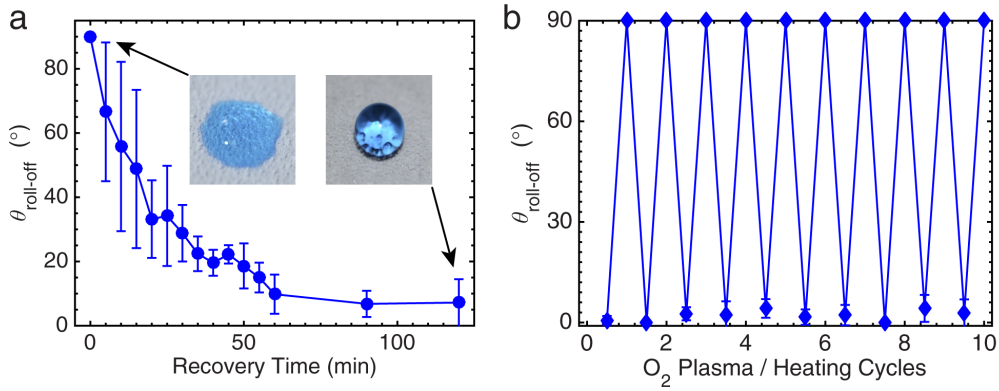

Figure 3.17: (*a*) The roll-off angle of the FPU + 15 wt% F-POSS coating after O_2 plasma treatment, as a function of recovery time at 80 °C. As the fully fluorinated chains bloomed to the surface, the surface energy decreased, and water was more easily repelled. The insets show water droplets (dyed blue) after O_2 plasma treatment, and after thermal recovery. (*b*) Successive O_2 plasma/recovery cycles, highlighting that the self-healing nature of the FPU/F-POSS coating was quite robust.

increasing temperature, consistent with a diffusion-controlled process. When the temperature was increased to 150 °C, complete recovery was observed within 20 min. Alternating treatments of the coating with O_2 plasma and 150 °C heat cycling showed that the superhydrophobicity could be repeatedly fully recovered (Figure 3.17b).

3.6.6 Corrosion Testing

Corrosion testing was done in accordance to the ASTM B117 standard.[144] Briefly, 25 mm × 75 mm mild steel substrates were spray-coated with the FPU + 15 wt% F-POSS coating. A 25 mm scratch was made along the length of the coating in the center of the sample so that the steel underneath was exposed. The coated pieces were hung in a salt-spray fog chamber (Bemco) held at 35 °C for 200 hours. After the accelerated corrosion, the contact angles were measured and found to have been

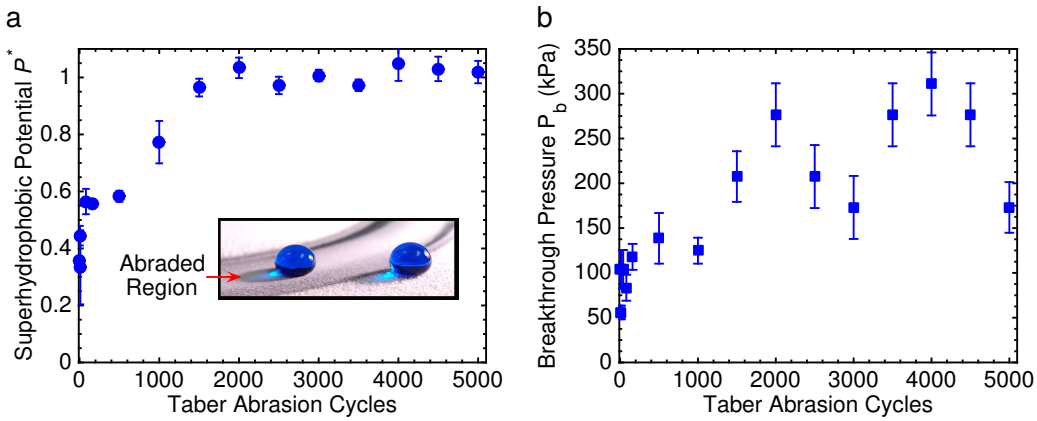

Figure 3.18: Capillary resistance. (*a*) The P^* parameter as a function of the number of abrasion cycles for the FPU/F-POSS coating after self-healing. The inset shows water droplets (dyed blue) displaying high contact angle even after 5,000 abrasion cycles. (*b*) The breakthrough pressure of the FPU/F-POSS coating as a function of abrasion, after self-healing.

negligibly impacted, and the coating prevented corrosion from spreading from the initial scratch (Figure 3.11)

3.6.7 Retention of Pressure Resistance

Even after mechanical wear, a robust SHS should also exhibit a large capillary resistance or breakthrough pressure, P_b, defined as the pressure required to force a transition from the Cassie-Baxter to the Wenzel state.[5,6,133,136,145,146] The FPU/F-POSS coating maintained $P^* < 1.0$ over 5,000 abrasion cycles (Figure 3.18a), indicating an energetically favorable Cassie-Baxter state, however, excessive applied pressures can still force an irreversible transition to the wetted Wenzel state.[5]

To evaluate the breakthrough pressure, we completely submerged our self-healed FPU/F-POSS coating in a water tank, applied pressure by injecting compressed air, and observed whether the sample was wetted after retrieving it from the tank. The breakthrough pressure of this coating was initially $P_b = 100 \pm 20$ kPa, and never decreased below $P_b = 50$ kPa, even after 5,000 abrasion cycles (Figure 3.18b). Remarkably, the pressure resistance increased to a maximum of $P_b = 310$ kPa after 4,000 abrasion cycles, due to the decrease in S_q with increasing abrasion. As such, even water droplets impinging the abraded surface at an impact velocity of 5.7 m/s completely rebounded, leaving the surface dry (Figure 3.19). In fact, the measured breakthrough pressure of 310 kPa corresponds to a droplet impact velocity of $V \approx 25$ m/s ($P_{Bernoulli} = \rho V^2/2$, where ρ is the fluid density), which is higher than the terminal velocity of a millimetric water droplet in air. Whereas SHSs often only maintain high water contact angles after mechanical damage, the surfaces reported here preserved all their advantageous water-repellent properties (high θ^*, $\theta_{roll\text{-}off} < 15°$, high P_b), even after harsh mechanical abrasion.

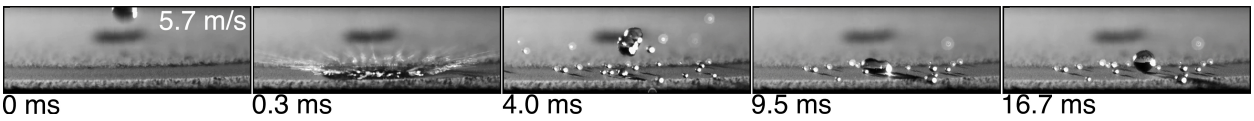

Figure 3.19: A water droplet, dropped from a height of 1.7 m, impacted the abraded region (4,000 abrasion cycles) of the FPU/F-POSS coating at a velocity of 5.7 m/s. After breaking up, the satellite droplet bounced at least four times after impacting the surface. The surface was tilted 1.5°.

3.7 Drag Reduction in Turbulent Flow

This section briefly describes a collaboration with Prof. Steven L. Ceccio, Prof. Marc Perlin, and James W. Gose in the Department of Naval and Marine Engineering, as part of a wider Office of Naval Research Multi-University Research Initiative. This work is published in the *Journal of Fluid Mechanics*.[147] Kevin Golovin and James Gose performed the majority of the skin-friction experiments, and extension to tow-tank testing is being undertaken with James Gose and Brian Tobelmann.

3.7.1 Introduction

One use of durable, scalable SHSs is drag reduction in turbulent flows relevant to marine applications.[148] Fuel consumption by ships is predicted to double between 2010 and 2030.[149] Nearly 60% of this fuel will be expended to overcome frictional skin drag on the wetted surface of vessels.[150] Hence, methods that can effectively reduce the frictional drag on marine vessels could have enormous global economic and environmental impact. Technologies including riblet, polymer, or air-layer drag reduction have all been considered for hydrodynamic drag reduction.[151,152] Active methods such as air or polymer injection require significant mass and energy input.[153–155] Therefore, passive methods to significantly reduce skin-friction drag in hydrodynamic flows at high Reynolds numbers are highly desirable. Researchers have consistently shown that SHSs can effectively lower frictional drag in laminar flow by allowing a non-zero slip velocity at the wall, due to the incorporated air fraction[1,156–167] However, the extension of frictional drag reduction to wall-bounded turbulent flows has not been straightforward.[153,156–158,168–172] The mechanism of these potentially drag-reducing surfaces has been previously debated and a very wide range of measured drag has been reported.[148,157,170,173,174]

3.7.2 Surfaces

In this work, we examined the physical properties that enable a superhydrophobic surface to reduce drag in turbulent flow. We then designed, fabricated, and several scalable surfaces, including the coating based on FPU/F-POSS discussed throughout the rest of this chapter (Figure 3.20, Table 3.5). These four surfaces were fabricated on stainless steel or polycarbonate substrates which were 1.20 m $\times$ 0.10 m, an order of magnitude larger than most other SHSs previously tested in turbulent

Table 3.5: Summary of the SHSs fabricated for this work, with their apparent contact angles, θ^*, and their root-mean-squared roughnesses, k.

Type	Description	θ^*	k
1	Sprayed FPU + F-POSS	163 ± 2°	18 ± 1.0 μm
2	Sprayed SF100 + F-POSS	161 ± 5°	6.4 ± 0.8 μm
2 (more rough)	Sprayed SF100 + F-POSS	161 ± 3°	8.5 ± 0.4 μm
2 (less rough)	Sprayed SF100 + F-POSS	167 ± 2°	2.7 ± 0.3 μm
3	Sprayed FPU + fluoro-silica	172 ± 2°	1.2 ± 0.2 μm
4	Etched, boiled, fluoro-silanized aluminum	170 ± 2°	4.7 ± 0.7 μm

flows.[153,156,168,171,172] These were tested for their capability to reduce drag in a fully-developed turbulent flow facility. While quite not as mechanically robust as surface #1, the other surfaces were largely resistant to damage caused by fast-flowing water in these experiments and retained their superhydrophobicity after testing.

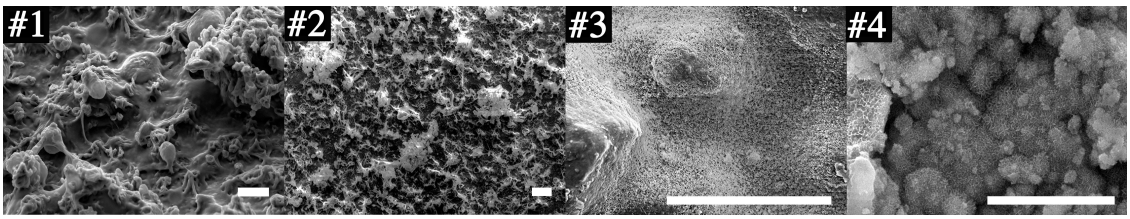

Figure 3.20: SEM micrographs of the four SHSs produced in this work. Scale bars are 20 μm.

3.7.3 Results

While all of these surfaces resisted complete wetting under the elevated shear flows during testing, the net effect on the drag compared to a hydraulically smooth surface varied from 90% reduction to 90% increase. The two key elements for superhydrophobic drag reduction identified during this work are: low contact angle hysteresis under elevated pressures and roughness below the viscous length scale of the turbulent flow. Surfaces with smaller texture features which maintained low wetted area even under elevated pressure were more likely to yield drag reduction (#2 (less rough), and the primarily nanotextured coatings #3 and #4) (Figure 3.21). However, surfaces like #1 and #2, with texture features up to 200 μm across, tended to increase drag even when they remained non-wetted. If the coating roughness elements are large compared to the purely viscous layer near the channel wall, turbulent eddies and vortices may be generated around the features protruding into the flow, causing drag increase. The viscous length scale is defined as $\delta_\nu \equiv \nu/u_\tau$,[175] where ν is the kinematic viscosity of the fluid and u_τ is the velocity at the wall. A non-dimensional surface roughness relative to this viscous length scale may then be formulated as $k^+ = k/\delta_\nu$. Conventionally, a surface is considered hydraulically rough once $k^+ > 5$,[175] but we observed drag increase well below this threshold, and drag reduction only on some of the surfaces with roughness well below the viscous

length scale ($k^+ < 1$). Combining k^+ with measurements of contact angle hysteresis at elevated pressures, $\Delta\theta^{HP}$ yielded a better predictive model for superhydrophobic surfaces that reduce drag.

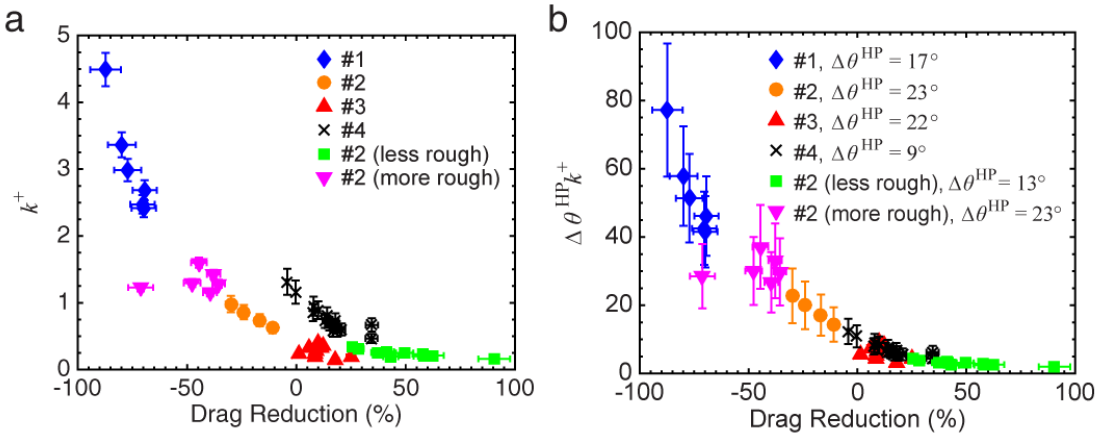

Figure 3.21: The effect of surface roughness on drag. (*a*) The net drag reduction (negative means increased drag) caused by all the surfaces as a function of their non-dimensional roughness, k^+. (*b*) The drag reduction data collapsed onto a single curve when plotted versus the product of the non-dimensional roughness and the higher-pressure contact angle hysteresis (370 Pa for a 250 nL droplet)

These experiments were performed in shallow enclosed channels, but it is necessary to test these coatings in the open-boundary conditions found on real vessels, which were believed to have larger viscous length scales and should tolerate higher coating roughness. Ongoing work is focused on testing these coatings on a DARPA Suboff submersible model in the Marine Hydrodynamics Laboratory tow tank. The findings in the skin-friction flow facility suggested that the optimal coating would be primarily nanotextured and relatively smooth. However, it proved to be relatively challenging to produce such coatings in a scalable manner on the Suboff while achieving damage and pressure resistance comparable to that of surface #1. Longevity under high shear flow was eventually achieved with a variant of surface #1 which was subsequently coated with surface #3 to fabricate a hierarchically textured coating, yielding a final $k \approx 30 \pm 4$ μm (Figure 3.22). These were successfully applied to the mid-body of the Suboff, which is a cylindrical aluminum section that is 1.5 m long and 0.3 m across (surface area ~12× that of the previous samples). The nanoscale texture of the coating remained non-wetted after testing up to velocities of 4 m/s at 1.5 m immersion depth over several hours, however the initially highly reflective and smooth entrapped air layer did conform to the microscale geometry soon after immersion at testing depth. This initial test on the relatively rough coating showed no significant effect on drag, suggesting that the viscous length scale of the Suboff geometry is far lower than initially thought, and the form drag increase counteracted any reduction in frictional drag. Subsequent experiments will focus on coatings with reduced microscale roughness to yield net drag reduction.

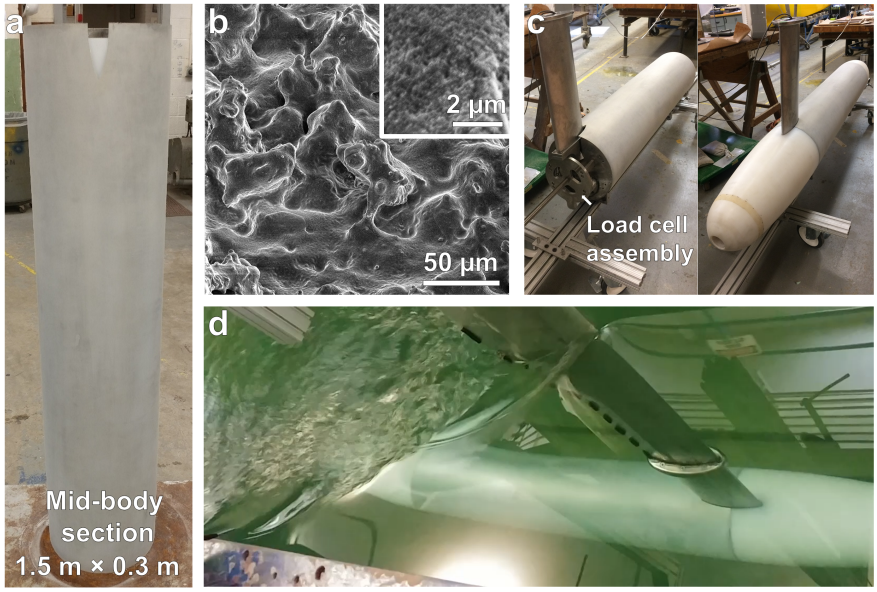

Figure 3.22: (*a*) The coated Suboff mid-body section. (*b*) SEM of the micro- and nano-structured hierarchical spray-coating composed of FPU+F-POSS overcoated with FPU+fluorosilica. (*c*) Assembly of the Suboff. (*d*) Tow-tank testing.

3.8 Conclusions

In summary, we have explored how miscibility between hydrophobic fillers and polymeric binders allows one to control the formation of surface texture during spray coating, in order to fabricate superhydrophobic surfaces. The S^* parameter quantifies the miscibility between the two sprayable components, and the P^* parameter characterizes the stability of the non-wetted state. Superhydrophobic surfaces should be designed such that $S^* < 1.0$, to afford mechanical durability, and $P^* < 1.0$, to provide a robust non-wetting state. Utilizing these two design criteria, we have fabricated superhydrophobic surfaces with unprecedented mechanical durability. Some of these surfaces also exhibited a self-healing nature, both chemically and physically, and were able to fully recover their superhydrophobicity after a wide variety of extreme chemical and physical exposures. These surfaces, and the design parameters used to develop them, may find immediate usage in a wide range of academic and industrial sectors across the globe. Since preliminary testing suggests that these solely microtextured surfaces may not be ideal for marine drag reduction applications, combining them with hierarchical nanotexture is the focus of ongoing work to fabricate coatings which may yield significant drag reduction under high-velocity turbulent flows.